

Nuclear Reactions in Evolving Stars (and their theoretical prediction)

Friedrich-Karl Thielemann * and Thomas Rauscher

Abstract This chapter will go through the important nuclear reactions in stellar evolution and explosions, passing through the individual stellar burning stages and also explosive burning conditions. To follow the changes in the composition of nuclear abundances requires the knowledge of the relevant nuclear reaction rates. For light nuclei (entering in early stellar burning stages) the resonance density is generally quite low and the reactions are determined by individual resonances, which are best obtained from experiments. For intermediate mass and heavy nuclei the level density is typically sufficient to apply statistical model approaches. For this reason, while we discuss all burning stages and explosive burning, focusing on the reactions of importance, we will for light nuclei refer to the chapters by M. Wiescher, deBoer & Reifarth (Experimental Nuclear Astrophysics) and P. Descouvemont (Theoretical Studies of Low-Energy Nuclear Reactions), which display many examples, experimental methods utilized, and theoretical approaches how to predict nuclear reaction rates for light nuclei. For nuclei with sufficiently high level densities we discuss statistical model methods used in present predictions of nuclear reaction cross sections and thermonuclear rates across the nuclear chart, including also the application to nuclei far from stability and fission modes.

Friedrich-Karl Thielemann
Department of Physics, University of Basel, Switzerland, and GSI Helmholtz Center for Heavy Ion Research, Darmstadt, Germany e-mail: f-k.thielemann@unibas.ch

Thomas Rauscher
Department of Physics, University of Basel, Switzerland, and Centre for Astrophysics Research, University of Hertfordshire, Hatfield, United Kingdom; ORCID:0000-0002-1266-0642 e-mail: thomas.rauscher@unibas.ch

* corresponding author

Describing nuclear composition changes via nuclear reaction rates

Before going into more details about the nuclear reactions in evolving stars in the next sections, we present here a short overview of the tools used to calculate abundances changes via nucleosynthesis networks and the relevant reaction rates. Abundances of nuclei can be defined by their mass fraction (X_i), i.e. the percentage of their mass in species i (or density ρ_i) with respect to the total mass (density) in two possible ways:

$$X_i = \frac{\rho_i}{\rho} = \frac{n_i m_i}{\rho} = \frac{n_i \mathcal{A}_i m_u}{\rho} = \frac{n_i}{(\rho/m_u)} \mathcal{A}_i \quad (1a)$$

$$X_i = \frac{n_i m_i}{\rho N_A} N_A = \frac{n_i}{\rho N_A} \mathcal{A}_i m_u N_A = \frac{n_i}{\rho N_A} \mathcal{A}_i M_u, \quad (1b)$$

with n_i being the number density, ρ the overall mass density, N_A the Avogadro number, $m_u = \frac{1}{12}m(^{12}\text{C})$ the nuclear mass unit, \mathcal{A}_i the relative atomic mass, and $M_u = N_A m_u$ the molar mass constant. Replacing the relative atomic mass \mathcal{A}_i by $A_i = N_i + Z_i$, i.e. the nuclear mass number given by the sum of neutrons and protons in a nucleus, introduces an error in the per-mille range due to the nuclear binding, which is usually neglected. The abundance of a nucleus, rather than its mass fraction, should not reflect its weight and is defined as $Y_i = X_i/\mathcal{A}_i \approx X_i/A_i$, which can be expressed, utilizing Eq.(1), by $Y_i = n_i/(\rho N_A) M_u = n_i/(\rho/m_u)$. Until 2019 M_u had the value of 10^{-3} kg/mole or 1 g/mole in cgs units. This led [Fowler et al \(1967\)](#) and the following literature to omit this factor of 1 in the definition of the abundance (but also introducing the dimension of g/mole). According to the latest CODATA evaluation ([Tiesinga et al, 2021](#), Table XXXI) this is still close to being correct (numberwise) with a precision of 3×10^{-10} , but introduces somewhat confusing dimensions for the abundances. We will continue to utilize here the traditional expressions, but want to make clear that, when changing all terms ρN_A - appearing in equations introduced here and later in this text - to ρ/m_u , like in $Y_i = n_i/(\rho/m_u)$ (as often done in more modern approaches, see e.g. [Cowan et al, 2021](#)), the expressions stay valid and lead for the mass fractions $X_i = A_i Y_i$ as well as the abundances Y_i to dimensionless numbers. All mass fractions add up to unity:

$$\sum_i X_i = \sum_i A_i Y_i = 1. \quad (2)$$

Astrophysical environments carry generally no charge, i.e. the total number of protons has to be equal to the number of electrons

$$\sum_i Z_i Y_i = Y_e = \frac{n_e}{\rho N_A}, \quad (3)$$

with the electron fraction (Y_e) being on the one hand defined by the electron number density but also equal to the number of protons per nucleon (i.e., protons plus neutrons) $Y_e = \sum_i Z_i Y_i / \sum_i A_i Y_i$.

The individual abundances can be calculated with a nuclear reaction network based essentially on r , the number of reactions per volume and time that can be expressed, when targets and projectiles follow specific distributions dn , by

$$r_{ij} = \int \sigma \cdot |\vec{v}_i - \vec{v}_j| dn_i dn_j. \quad (4)$$

The evaluation of this integral depends on the type of particles and distributions which are involved. For nuclei i and j in an astrophysical plasma, obeying a Maxwell–Boltzmann distribution we find $r_{ij} = n_i n_j \langle \sigma v \rangle_{ij}$ where $\langle \sigma v \rangle$ is integrated over the relative bombarding energy and is only a function of temperature T

$$\langle \sigma v \rangle_{ij}(T) = \left(\frac{8}{\pi \mu_{ij}} \right)^{1/2} (kT)^{-3/2} \int_0^\infty E \sigma(E) \exp\left(-\frac{E}{kT}\right) dE, \quad (5)$$

where μ_{ij} is the reduced mass of target and projectile i and j . For a reaction with photons we have $j = \gamma$, i.e. in this case the projectile j is a photon. The relative velocity is the speed of light c , the distribution dn_j is the Planck distribution of photons. As the relative velocity between the nucleus and the photon is a constant (c), and the photodisintegration cross section is only dependent on the photon energy E_γ , the integration over dn_i can be easily performed, resulting in

$$\begin{aligned} r_{i\gamma} &= n_i \frac{1}{\pi^2 c^2 \hbar^3} \int \frac{\sigma_i(\gamma; E_\gamma) E_\gamma^2}{\exp(E_\gamma/kT) - 1} dE_\gamma = n_i \lambda_{i\gamma}(T) \\ \lambda_{i\gamma}(T) &= \frac{1}{\pi^2 c^2 \hbar^3} \int \frac{\sigma_i(\gamma; E_\gamma) E_\gamma^2}{\exp(E_\gamma/kT) - 1} dE_\gamma. \end{aligned} \quad (6)$$

Contrary to the reactions among nuclei or nucleons, where both reaction partners are following a Boltzmann distribution, this expression has only a linear dependence on number densities. The integral acts like an effective (temperature dependent) decay constant of nucleus i . Electron captures behave in a similar way as the mass difference between nucleons/nuclei and electrons is huge and the relative velocity is with high precision given by the electron velocity. This leads to

$$r_{i:e} = n_i \int \sigma_e(v_e) v_e dn_e = \lambda_{i:e}(\rho Y_e, T) n_i. \quad (7)$$

This is an expression similar to that for photodisintegrations, but now we have a temperature and density dependent “decay constant”, because the electron distribution has also a density dependence and can change to a degenerate Fermi gas (for details see the chapter by Suzuki and [Langanke et al \(2021\)](#)). In principle neutrino reactions with nuclei would follow the same line, because the neutrinos, propagating

essentially with light speed, would lead to a simple integration over the neutrino energies. However, as neutrinos, interacting very weakly, do not necessarily obey a thermal distribution for local conditions, their spectra depend on detailed transport calculations (see the chapters by Rrapaj & Reddy, Fuller & Grohs, Wang & Surman, Famiano et al., Fröhlich, Wanajo, and Obergaulinger), leading to

$$r_{i\nu} = n_i \int \sigma_e(E_\nu) c dn_\nu(E_\nu) = \lambda_{i\nu}(\text{transport}) n_i. \quad (8)$$

Finally, for normal decays, like beta- or alpha-decays or ground-state fission with a half-life $\tau_{1/2}$, we obtain a similar equation with a decay constant $\lambda_i = \ln 2 / \tau_{1/2}$ (see the chapter by Rubio et al., Block et al., Oberstedt & Oberstedt, Schunk, and Kowal & Skalski) and

$$r_i = \lambda_i n_i. \quad (9)$$

In this case the change of the number density due to decay is $\dot{n}_i = -\lambda_i n_i$, with the solution $n_i = n_i(0) e^{-\lambda_i t}$ and $n_i(\tau_{1/2}) = \frac{1}{2} n_i(0)$. The decay half-life of a nuclear ground state is a constant.

Adding all these different kind of reactions, we can describe the time derivative of abundances $Y = n/\rho N_A$ as the difference of production and destruction terms with a differential equation for each species. Both the production and destruction channels include particle-induced reactions, decays, photodissociation, electron capture, etc. For every nucleus i the abundance is given by a differential equation

$$\begin{aligned} \dot{Y}_i = & \sum_j N_j^i \lambda_j Y_j + \sum_{j,k} \frac{N_{j,k}^i}{1 + \delta_{jk}} \rho N_A \langle \sigma v \rangle_{j,k} Y_j Y_k + \\ & \sum_{j,k,l} \frac{N_{j,k,l}^i}{1 + \Delta_{jkl}} \rho^2 N_A^2 \langle \sigma v \rangle_{j,k,l} Y_j Y_k Y_l, \end{aligned} \quad (10)$$

where the factors $1/(1 + \delta_{jk})$ and $1/(1 + \Delta_{jkl})$ prevent double counting of reactions in two- and three-body reactions, respectively. Δ_{jkl} has the value 0, 1 or 5, so that, dependent on the multiplicity of identical partners, the denominators are equal to 1!, 2!, or 3!. For methods to solve these (often huge) stiff sets of ordinary differential equations see e.g. [Hix and Thielemann \(1999\)](#) and [Timmes \(1999\)](#), a general overview of utilized codes in astrophysical applications as well as of publicly available tools is given in [Reichert et al \(2023\)](#).

Knowing the cross section $\sigma(E)$ of a nuclear reaction, $\langle \sigma v \rangle$ can easily be determined, provided that the participating nuclei obey Boltzmann statistics. In the following section we want to utilize this method to predict abundance/composition changes. We will first go through the stellar burning stages identifying the important reactions, while we rely on the sections by M. Wiescher and P. Descouvement how they are determined experimentally or theoretically for light nuclei, before introducing statistical model methods for intermediate mass and heavy nuclei.

One extreme case should however be mentioned, which occurs at sufficiently high temperatures when on the one hand the Coulomb barriers can be overcome for capture reactions and on the other hand the reverse photodisintegrations are efficient due to the high energy photons of the corresponding Planck distribution. For a reaction $i(p, \gamma)m$, with i standing for nucleus (Z, A) and m for $(Z + 1, A + 1)$, the relation between the forward rate $\langle \sigma v \rangle_{i;p,\gamma}$ and the photodisintegration rate $\lambda_{m;\gamma,p}$ is given by

$$\lambda_{m;\gamma,p}(T) = \frac{g_p G_i}{G_m} \left(\frac{\mu_{in} kT}{2\pi\hbar^2} \right)^{3/2} \exp(-Q_{i;p,\gamma}/kT) \langle \sigma v \rangle_{i;p,\gamma}, \quad (11)$$

containing the reduced mass μ_{in} and the capture Q-value for the reaction, $g_p = 2 \times (1/2) + 1$ for the protons and the partition functions G for the nuclei involved. When utilizing that the difference between forward proton capture and backward photodisintegration flux for nucleus i , i.e. $\dot{Y}_i = -\rho N_A \langle \sigma v \rangle_{i;p,\gamma} Y_p Y_i + \lambda_{m;\gamma,p} Y_m$ vanishes in chemical equilibrium. Making also use of the relation between $\langle \sigma v \rangle_{i;p,\gamma}$ and $\lambda_{m;\gamma,p}$, based on detailed balance, results in

$$\frac{Y_m}{Y_i} = \rho N_A Y_p \frac{G_m}{2G_i} \left[\frac{A_m}{A_i} \right]^{3/2} \left[\frac{2\pi\hbar^2}{m_u kT} \right]^{3/2} \exp\left(\frac{Q_{i;p,\gamma}}{kT}\right). \quad (12)$$

Such a chemical equilibrium for a specific forward and reverse reaction can also apply for e.g. neutron or even alpha captures. When temperatures are sufficiently high to permit a whole sequence of proton and neutron captures up to nucleus (Z, A) or (Z, N) , a complete chemical equilibrium (also termed nuclear statistical equilibrium NSE) can be attained, linking neighboring nuclei via neutron or proton captures as in Eq.(12) up to nucleus (Z, N) . The approach to such NSE conditions is discussed in the following section on burning phases in stellar evolution.

It is important to note that the reaction cross sections appearing in Eqs. (4) – (8), as well as the reactivities $\langle \sigma v \rangle$ in Eq. (10) must account for the thermal excitation of nuclei in an astrophysical plasma and may differ from laboratory cross sections, determining cross sections of target nuclei in their ground states only. In an astrophysical environment, nuclei are found in excited states with a probability given by the plasma temperature T and the excitation energies E_i of low-lying excited states (Ward and Fowler, 1980). Thus, the actual *stellar* reaction rate r^* is given by a weighted sum of rates of reactions on individual excited states bombarded by a thermal (or non-thermal, in case of neutrinos) distribution of projectiles (Rauscher, 2020),

$$r^* = P_0 r_0 + P_1 r_1 + P_2 r_2 + \dots, \quad (13)$$

with the individual population factor of an excited state given by

$$P_i = \frac{2J_i + 1}{G} e^{-E_i/(kT)}. \quad (14)$$

Here, G is the nuclear partition function of the target nucleus and J_i the spin of excited state i ($i = 0$ for the ground state). The reciprocity relation shown in Eq. (11) also only holds when such stellar rates are used. Instead of summing over individual contributions from several rate integrals as shown in Eq. (13), the form of a single integral (as in Eq. 4) can be retained by using a stellar cross section σ^* as defined in Eq. (26) (Holmes et al, 1976; Rauscher, 2020, 2022).

The relative contribution to the stellar rate of reactions on nuclides in the ground state can be computed from

$$X_0^*(T) = \frac{r_0}{r^*G}, \quad (15)$$

where r_0 is the reaction rate calculated from reactions on the ground state only. Since the population of excited states depends on the excitation energies of available excited states, the impact of excited states is smaller (and thus $X_0 \approx 1$) for light nuclides with large level spacings but is non-negligible ($X_0 < 1$) for intermediate and heavy nuclides even at such low temperatures $k_b T$ of a few keV, as encountered, e.g., in the s-process (Rauscher, 2022). In hot, explosive astrophysical environments X_0 becomes tiny and most contributions to the stellar rate come from reactions on excited states.

Stellar burning stages

Stellar burning stages are characterized by reactions involving increasingly larger nuclei (and charges). The necessary velocities (energies) to overcome the Coulomb barriers of heavier nuclei increase with charge Z and are related to the environment temperature. When one type of reaction sequence is started, the energy loss of a star (its luminosity) is equal to the total energy generation, once stable burning conditions have been attained. The burning temperature stays approximately constant until the fuel is exhausted. At that point decreasing pressure support will lead to a contraction, which again causes a temperature increase, due to the release of gravitational binding energy. At some critical temperature threshold the nuclei of the next burning “fuel” can overcome the Coulomb barriers in the main reactions of this next burning stage. In massive stars the sequence of burning stages is given by the fuels ^1H , ^4He , ^{12}C , ^{20}Ne , ^{16}O and ^{28}Si (see also the chapter by K. Nomoto on the impact of reaction rate uncertainties on stellar evolution). We want to discuss the details and the main reaction sequences of all these burning stages in the following subsections.

Table 1 The PP-Cycles in Hydrogen Burning

cycle	reaction	τ (years)	Q(MeV)
PPI	${}^1\text{H}(p, e^+ \nu) {}^2\text{H}$	7.9×10^9	0.420
(pep reaction)	${}^1\text{H}(pe^-, \nu) {}^2\text{H}$	3.7×10^{12}	1.442
	${}^2\text{H}(p, \gamma) {}^3\text{He}$	5.9×10^{-8}	5.493
	${}^3\text{He}({}^3\text{He}, 2p) {}^4\text{He}$	$1.4/Y_3$	12.859
PPII	${}^3\text{He}(\alpha, \gamma) {}^7\text{Be}$	1.1×10^6	1.586
	${}^7\text{Be}(e^-, \nu) {}^7\text{Li}$	2.9×10^{-1}	0.861
	${}^7\text{Li}(p, \alpha) {}^4\text{He}$	4.3×10^{-5}	17.347
PPIII	${}^7\text{Be}(p, \gamma) {}^8\text{B}$	1.8×10^2	0.135
	${}^8\text{B}(e^+ \nu) {}^8\text{Be}^*(\alpha) {}^4\text{He}$	3.5×10^{-8}	18.078
PPIV (Hep reaction)	${}^3\text{He}(p, e^+ \nu) {}^4\text{He}$	3.7×10^7	19.795

Hydrogen Burning

The PP-Cycles

In a pure hydrogen gas the reaction sequences in Table 1 occur at $T \approx 10^7$ K. We give the individual sub-cycle name, the Q-value and a lifetime for each reaction. Although the purely nuclear Q-value of the first pp-reaction is only 0.420 MeV, the effective Q-value is also 1.442 MeV as in the pep-reaction, because the positron annihilates with an electron in the plasma and produces 1.022 MeV in photons. In the case of a decay, lifetimes are related to the decay constant λ via $\tau = 1/\lambda$, or half-life with $\lambda = \ln(2)/\tau_{1/2}$. After a lifetime τ passed in a reservoir of unstable nuclei, a fraction $1/e$ will remain. For reactions involving a projectile and target, the target lifetime τ_i is given by $\dot{Y}_i = -\frac{1}{\tau_i} Y_i$, containing the reaction rate (i.e. requiring a knowledge of density and temperature) and the projectile abundance. The table values were obtained assuming $\rho = 100 \text{ g cm}^{-3}$, and $T = 1.5 \times 10^7 \text{ K}$, based on reaction rate evaluations of Angulo et al (1999) and Adelberger et al (2011). The abundances are taken from an intermediate state of H-burning with $Y_{\text{H}} = 0.5$, $Y_{\text{He}} = 0.5/4$ (i.e. half of the H is burned to He), while in a steady flow equilibrium the abundances of the intermediate nuclei are close to negligible. For most of the reactions in Table 1 the projectile is either ${}^1\text{H}$ or ${}^4\text{He}$, i.e. the lifetimes can be determined with these known abundances, an exception is ${}^3\text{He}({}^3\text{He}, 2p) {}^4\text{He}$. When taking typical steady flow values of the order $Y_3 = Y_{3\text{He}} \approx 10^{-4}$, this leads to a lifetime of about 10^4 years.

In all cases (i.e. PPI, PPII, PPIII or PPIV) the net reaction is the fusion of 4 protons into one alpha particle (${}^4\text{He}$) with two β -decays or electron captures among the intermediate reactions. In the PPI-cycle six hydrogen nuclei (protons) are required in total, two are finally released in the ${}^3\text{He}$ - ${}^3\text{He}$ -reaction, together with one helium nucleus, i.e. the net reaction is $4 {}^1\text{H} \rightarrow {}^4\text{He}$. The slowest reaction (of relevance) in all the cycles is the first one listed. The pep-reaction is the slowest of all, because a three body collision is a very rare event. It is, however, unimportant for H fusion, as the pp-reaction burns and produces the same nuclei, only the properties of the emitted neutrinos are different.

The PPIV cycle or Hep reaction is mostly important for relatively high energy neutrinos, but, as can be seen from the lifetime of the Hep reaction in comparison to ${}^3\text{He}(p,\gamma)$, it carries also about one third of the latter PPII flux from ${}^3\text{He}$ to ${}^4\text{He}$. The pp-reaction is very slow, because a diproton (${}^2\text{He}$) is unstable and breaks up immediately. During the very limited time of the existence of a diproton a weak transition of one of the protons into a neutron occurs. The production of deuterium (${}^2\text{H}$) is only possible during the very limited time of the existence of a diproton, when a weak transition of one of the protons into a neutron occurs. Due to its rarity, this reaction rate is based entirely on theoretical predictions. A cross section that small is not accessible by experiments. It should, nevertheless, be quite accurate, because only the fundamental constants of weak interaction theory enter. Thus a description of nuclear many body systems (nuclei), which may or may not be correct, is not required (see the detailed discussion in e.g. [Rolfs and Rodney, 1988](#); [Bahcall, 1989](#); [Adelberger et al, 2011](#)).

The other pp-cycle reactions are studied by experiments (see for historical reasons the detailed discussions in [Rolfs and Rodney, 1988](#)), [Caughlan and Fowler \(1988\)](#) and updates in [Angulo et al \(1999\)](#) and [Adelberger et al \(2011\)](#)). Typically, cross-sections are measured at somewhat higher energies, where cross sections are larger and then extrapolated to the solar energies of interest (see e.g. [Formicola et al, 2016](#)). There existed some uncertainty in the reaction ${}^7\text{Be}(p,\gamma){}^8\text{B}$, but recent evaluations by [Tursunov et al \(2021\)](#) provide nice agreement with the [Adelberger et al \(2011\)](#) rate. ${}^7\text{Be}$ is unstable against electron capture (EC), not β^+ -decay, due to a small Q-value. The terrestrial lifetime, $\tau=77\text{d}$ (half life $\tau_{1/2}=53\text{d}$), is caused by capture of a bound K-shell electron. For conditions in the center of stars, where atoms are completely ionized, electron capture has to occur with electrons from the continuum electron distribution, which leads to a lifetime of 106d for the conditions of [Table 1 \(Adelberger et al, 2011\)](#). The terrestrial lifetime is long enough to produce radioactive ${}^7\text{Be}$ targets and several direct measurements of the ${}^7\text{Be}(p,\gamma){}^8\text{B}$ reaction have been performed by radioactive ion beam facilities (see e.g. [Adelberger et al, 2011](#)). In such a case ${}^7\text{Be}$, produced by a primary nuclear reaction, is accelerated in a second step onto an existing hydrogen gas target. Thus, the role of target and projectile is reversed and the reactions.

After a burning cycle proceeds for a time scale in excess of all reaction time scales in the cycle, except for the longest one, an abundance equilibrium is attained. In general such a situation is called a steady flow equilibrium, where the slowest link determines the speed and all other reactions adjust to that reaction flow. The destruction of ${}^1\text{H}$ (and the build-up of ${}^4\text{He}$) is caused, in temperature and density dependent fractions, by the four PP cycles, determined by the branch points at ${}^3\text{He}$ and ${}^7\text{Be}$, which open the PPII, PPIV and PPIII-cycles respectively. Only the latter branching is temperature and density dependent, because a decay [${}^7\text{Be}(e^-, \nu){}^7\text{Li}$] and a capture reaction have a different density dependence. Knowing the hydrogen abundance at a given time (and the density and temperature for determining the reaction rate) automatically determines the steady flow abundances of ${}^2\text{H}$ and ${}^3\text{He}$. From [Table 1](#) and the destruction time scales we see that only A=1 and 4 can have non-negligible abundances, more than four orders of magnitude larger than those of

any other cycle member. Mass conservation gives $Y_4 = (1 - Y_1)/4$. As can be seen from Table 1, the much larger lifetime of ^3He in the Hep reaction by 2-3 orders of magnitude make the PPIV cycle contribution unimportant for energy generation, but this sub-cycle can contribute the neutrinos with the highest energies.

The CNO-Cycles

If heavier elements (CNO) are already present in the stellar plasma, another chain of reactions is possible, when temperatures are large enough to permit the penetration of the larger Coulomb barriers. These reactions can be faster at appropriate temperatures than the weak pp-reaction which involves a $p(e^+\nu)n$ transition. Such a sequence of reactions, involving the most abundant lightest nuclei beyond ^4He (C, N, and O), are known as the CNO-cycles.

Table 2 The CNO-Cycles in Hydrogen Burning

cycle	reaction sequence
CNOI	$^{12}\text{C}(p,\gamma)^{13}\text{N}(e^+\nu)^{13}\text{C}(p,\gamma)^{14}\text{N}(p,\gamma)^{15}\text{O}(e^+\nu)^{15}\text{N}(p,\alpha)^{12}\text{C}$
CNOII	$^{15}\text{N}(p,\gamma)^{16}\text{O}(p,\gamma)^{17}\text{F}(e^+\nu)^{17}\text{O}(p,\alpha)^{14}\text{N}$
CNOIII	$^{17}\text{O}(p,\gamma)^{18}\text{F}(e^+\nu)^{18}\text{O}(p,\alpha)^{15}\text{N}$
CNOIV	$^{18}\text{O}(p,\gamma)^{19}\text{F}(p,\alpha)^{16}\text{O}$

Most of the reactions listed in Table 2 are also studied experimentally, but again the extrapolation to low energies in the keV range is important to understand the behavior at Gamow peak energies (see e.g. Adelberger et al, 2011). A major uncertainty has been the $^{17}\text{O}(p,\alpha)^{17}\text{O}(p,\gamma)$ -branching between the CNOII and CNOIII cycle, related mostly to a low-lying 65keV resonance (see e.g. Rolfs and Rodney, 1988) which has recently been determined by Bruno et al (2016) in a direct measurement. The CNOIV-chain is not of great importance at all temperatures, the flux is more than a factor 100 smaller than in the CNOIII-chain. At lower temperatures we have only one single chain without branchings, which is the CNOI chain. Therefore, the flux passing through each reaction in case of a steady flow equilibrium, $C = \rho N_A \langle i1 \rangle Y_i Y_1$, must be identical. $^{14}\text{N}(p,\gamma)^{15}\text{O}$ has the smallest reaction rate, which means that the larger rates for other reactions have to be balanced with smaller abundances and almost negligible abundances of the other CNO nuclei remain. In this case, when assuming initial solar abundances for all CNO-nuclei, a steady-flow equilibrium assembles all CNO nuclei in ^{14}N . This leads to

$$Y_{14} \approx \frac{X_{CNO}}{14}, \quad (16)$$

Solar system abundance determinations have changed in recent years. While meteoritic measurements help to determine the relative abundances of non-volatile elements, when requiring the ratio to H and He also solar spectra have to be analyzed. Early 1D spherically symmetric approaches of the solar photosphere have been

replaced by multi-dimensional 3D analyses (Anders and Grevesse, 1989; Asplund et al, 2009). This led to a change for X_{CNO} , i.e. the mass fraction of all CNO nuclei in a solar composition, from 1.4×10^{-2} to 9.33×10^{-3} (which is the mass fraction of all CNO nuclei in a solar composition with $Y_C = 2.18 \times 10^{-4}$, $Y_N = 5.73 \times 10^{-5}$, $Y_O = 3.7 \times 10^{-4}$ and $X_{CNO} = 12Y_C + 14Y_N + 16Y_O$, see e.g. Amarsi et al, 2021).

For solar CNO-abundances ($Y_{14} = 9.33 \times 10^{-3}/14$) and $Y_1 = 0.5$, the CNO-cycles dominate over the PP-cycles beyond $T = 1.75 \times 10^7$ K. Under solar conditions the PP-chains dominate by more than one order of magnitude. As in the PP-cycles the final product of H-burning is ${}^4\text{He}$. Essentially all initial CNO abundances are transferred to ${}^{14}\text{N}$, with none being burned to heavier nuclei. It is important to note that the CNO nuclei only act as a catalysts.

A cycle similar to the CNO cycle, requiring slightly higher temperatures is the NeNaMg-cycle, shown in Table 3.

Table 3 The NeNaMg-Cycles in Hydrogen Burning

cycle	reaction sequence
NeNaMgI	${}^{20}\text{Ne}(p,\gamma){}^{21}\text{Na}(e^+\nu){}^{21}\text{Ne}(p,\gamma){}^{22}\text{Na}(p,\gamma){}^{23}\text{Mg}(e^+\nu){}^{23}\text{Na}(p,\alpha){}^{20}\text{Ne}$
NeNaMgII	${}^{21}\text{Na}(p,\gamma){}^{22}\text{Mg}(e^+\nu){}^{22}\text{Na}$

For updates beyond the compilations mentioned above (Angulo et al, 1999; Adelberger et al, 2011) see the impressive recent activities in underground labs which attempt to measure the related cross sections down to the relevant stellar energies: i.e. ongoing investigations in LUNA², CASPAR³ and JUNA (Liu et al, 2022), which avoid background noise and permit cross section measurements down to energies in the 50 keV region. This also applies for reactions of interest in the upcoming sections of He- and C-burning.

Helium Burning

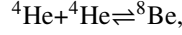
Main Reactions

There is no stable $A = 5$ nucleus. Proton or neutron captures on ${}^4\text{He}$ cannot produce heavier nuclei in stellar environments. This is the reason why hydrogen burning does not proceed beyond ${}^4\text{He}$. The ashes of hydrogen burning consist almost entirely of ${}^4\text{He}$, except for minor amounts of ${}^2\text{H}$, ${}^3\text{He}$, ${}^7\text{Li}$, and pre-existing heavy elements. ${}^3\text{He}({}^4\text{He}, \gamma){}^7\text{Be}$ produces ${}^7\text{Be}$ and, after decay, ${}^7\text{Li}$. In hydrogen burning Li is destroyed again via ${}^7\text{Li}(p, \alpha){}^4\text{He}$; in helium burning the small abundance of ${}^3\text{He}$

² <https://luna.lngs.infn.it/index.php/new-about-us>

³ <https://caspar.nd.edu/>

left over from hydrogen burning is exhausted very fast. The only reaction possible among ${}^4\text{He}$ -nuclei is



which produces the unstable ${}^8\text{Be}$ nucleus, decaying on a timescale of $2.6 \times 10^{-16}\text{s}$ via α -emission. However, increasing temperatures and densities lead to a large production of ${}^8\text{Be}$, which decays immediately, but a tiny abundance remains in (chemical) equilibrium (where forward and backward reaction cancel), leading to (with 4 and 8 standing for ${}^4\text{He}$ and ${}^8\text{Be}$)

$$\dot{Y}_8 = \frac{1}{2} \rho N_A \langle 4, 4 \rangle Y_4^2 - \lambda_8 Y_8 = 0 \quad \lambda_8 = \frac{1}{\tau_8} \quad \Gamma_8 \tau_8 = \hbar \quad \lambda_8 = \frac{\Gamma_8}{\hbar}. \quad (17)$$

The life time of ${}^8\text{Be}$ is related to the width of the ground state via the Heisenberg uncertainty principle. The equilibrium abundance of ${}^8\text{Be}$ is consequently

$$Y_8 = \frac{\hbar}{2\Gamma_8} \rho N_A \langle 4, 4 \rangle Y_4^2.$$

Another alpha-capture can follow, leading to the production of ${}^{12}\text{C}$

$$\begin{aligned} \dot{Y}_{12} &= \rho N_A \langle 4, 8 \rangle Y_4 Y_8 \\ &= \frac{\hbar}{2\Gamma_8} \rho^2 N_A^2 \langle 4, 4 \rangle \langle 4, 8 \rangle Y_4^3 \\ &\equiv \frac{1}{3!} \rho^2 N_A^2 \langle 4, 4, 4 \rangle Y_4^3. \end{aligned} \quad (18)$$

The last line is the definition of the triple-alpha-rate, treating it as if it were a real three-body reaction. In the case of a collision of three identical particles, we would have a double counting of possible reactions by taking the full helium abundance. The overcount is given by the permutations of the three particles, which would all end up in the same final ${}^{12}\text{C}$ nucleus, whatever the reaction sequence is. The number of permutations among three particles is $3!$, and thus is included in the above definition. This leads to the triple-alpha-reaction rate

$$\begin{aligned} &{}^4\text{He}(2\alpha, \gamma){}^{12}\text{C} \quad Q = 6.445 \text{ MeV} \\ N_A^2 \langle 4, 4, 4 \rangle &= N_A^2 \frac{3\hbar}{\Gamma_8} \langle 4, 4 \rangle \langle 4, 8 \rangle. \end{aligned} \quad (19)$$

A new feature is encountered in the triple-alpha reaction sequence which does not occur in regular two-dody reactions. The second alpha capture proceeds on a target in an unstable state with a natural width. If ${}^8\text{Be}$ was not produced at the resonance energy, but in the low energy tail, the energetics of the second alpha capture (with target ${}^8\text{Be}$) would be changed with respect to resonances in ${}^{12}\text{C}$. An appropriate approach (especially of importance at relatively low temperatures and high densities) which is also important in other applications, like explosive H-burning, has been

outlined in a number of publications (see e.g. [Nomoto et al, 1985](#); [Görres et al, 1995](#)).

A possible alpha capture reaction on the product ^{12}C depends on T , with

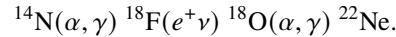
$$^{12}\text{C}(\alpha, \gamma)^{16}\text{O} \quad Q = 7.161 \text{ MeV}.$$

$^{16}\text{O}(\alpha, \gamma)^{20}\text{Ne}$ is blocked by a very small cross section, due to missing resonances at the appropriate energies in ^{20}Ne . Thus, the dominant ash of hydrogen burning (^4He) is burned in helium burning to ^{12}C and ^{16}O .

For typical burning conditions of $T = (1-2) \times 10^8 \text{ K}$ and $\rho = 3 \times 10^2 - 10^4 \text{ g cm}^{-3}$ the result is a mixture of ^{12}C and ^{16}O , with ^{16}O dominant at higher temperatures. This situation is, however, complicated by additional aspects of stellar evolution and overshadowed by a large experimental uncertainty of the $^{12}\text{C}(\alpha, \gamma)^{16}\text{O}$ cross section (see e.g. [deBoer et al, 2017](#), and the footnotes at the end of the H-burning section). The effectiveness of the $^{12}\text{C}(\alpha, \gamma)^{16}\text{O}$ reaction depends on the temperature of He-burning, i.e. the stellar mass *and* the cross section of the reaction itself. Since the temperature increases during He-burning, it is also important to note that the mixing of fresh He into the burning core, at the end of the core burning phase, can mimic a high reaction rate. Thus, the astrophysical treatment of convection is also important in this case. All of these effects contribute to the “effective” transformation of ^{12}C into ^{16}O . The C/O-ratio at the end of He-burning determines the further evolution of the star. Small carbon concentrations, or completely depleted carbon, can result in the case that either of the two burning stages of C-burning and Ne-burning is not occurring (for a detailed discussion see e.g., [Ojima et al, 2018](#), or the chapter by K. Nomoto).

Neutron Production in Helium Burning

Essentially all material in CNO-nuclei, present in the initial stellar composition, is processed to ^{14}N during hydrogen burning. This leads to a side branch of helium burning



This is the one reaction in helium burning, where protons are changed to neutrons, leading to a decrease of Y_e . For a solar initial composition with 1.4% by mass in CNO nuclei (which turned into ^{14}N in hydrogen burning), an abundance of $Y(^{22}\text{Ne}) = Y(^{14}\text{N}) = 0.014/14 = 1.0 \times 10^{-3}$ is obtained. This non-symmetric nucleus is characterized by $N - Z = 2$ and results in $Y_e = 0.499$.

Some of the ^{22}Ne undergoes another alpha-capture to produce ^{26}Mg . A smaller fraction (dependent on temperature) follows an endoenergetic reaction $^{22}\text{Ne}(\alpha, n)^{25}\text{Mg}$ ($Q = -0.482 \text{ MeV}$), i.e. only alpha energies (center of mass) beyond 0.482 MeV can induce this reaction. Such energies can be attained for $T > 3.5 \times 10^8 \text{ K}$. This is larger than the temperatures in helium burning discussed above. On the other hand, the energy threshold does not have to be at the center of the Gamow window of Eq.(5). The high energy tail also gives a contribution. It is clear, however, that

this neutron producing reaction is only active in late phases of core helium burning, which experience high temperatures.

When helium burning occurs in burning shells and shell flashes (to be discussed later), additional features can occur. High temperatures can be attained, and in some cases hydrogen is mixed into the helium burning zones, as a result of thermal pulses (or helium shell flashes). This permits proton captures on ^{12}C , which produce ^{13}N , decaying to ^{13}C . The latter is also a very efficient neutron source as due to a strong (α, n) -reaction. Both neutron sources (^{22}Ne and ^{13}C) lead to neutron production and the build-up of heavy elements via neutron capture and β^- -decay of unstable nuclei. If neutron capture time scales are longer than beta-decay time scales, this is called a slow neutron capture process (s-process), which will be discussed later in more detail. The important reactions are summarized in Table 4. As neutron capture cross sections increase with mass number, neutron captures occur preferentially on the most abundant heavy nucleus, i.e. ^{56}Fe . Some intermediate mass nuclei, which are produced in important quantities due to the ^{22}Ne neutron source and neutron capture chains based on it, are ^{21}Ne , ^{22}Ne , ^{25}Mg , ^{26}Mg , ^{36}S , ^{37}Cl , ^{40}K , and ^{40}Ar . The status of uncertainties in He-burning reactions, especially with respect to (α, n) - and (n, γ) -reactions, is discussed in Käppeler et al (2011); Febbraro et al (2020), but see also the footnotes at the end of the subsection on H-burning.

Table 4 Major Reactions in Helium Burning

(a) basic energy generation
$^4\text{He}(2\alpha, \gamma)^{12}\text{C}$ $^{12}\text{C}(\alpha, \gamma)^{16}\text{O}[(\alpha, \gamma)^{20}\text{Ne}]$
(b) neutron sources
$^{14}\text{N}(\alpha, \gamma)^{18}\text{F}(e^+ \nu)^{18}\text{O}(\alpha, \gamma)^{22}\text{Ne}$ $^{22}\text{Ne}(\alpha, n)^{25}\text{Mg}$
$^{12}\text{C}(p, \gamma)^{13}\text{N}(e^+ \nu)^{13}\text{C}(\alpha, n)^{16}\text{O}$
(c) high temperature burning with neutron sources
$^{22}\text{Ne}(n, \gamma)^{23}\text{Ne}(e^- \bar{\nu})^{23}\text{Na}(n, \gamma)^{24}\text{Na}(e^- \bar{\nu})^{24}\text{Mg}$
$^{20}\text{Ne}(n, \gamma)^{21}\text{Ne}(\alpha, n)^{24}\text{Mg}$
further s-processing via neutron captures and β -decays $^{24}\text{Mg}(n, \gamma)^{25}\text{Mg}$ etc.
production of heavy elements $^{56}\text{Fe}(n, \gamma)^{57}\text{Fe}(n, \gamma)^{58}\text{Fe}$ etc.

Carbon, Neon, and Oxygen Burning

Carbon Burning

We want to point out here that stars less massive than about $8M_{\odot}$ end their core evolution after helium burning. They become (electron-)degenerate and do not contract further due to the electron degeneracy pressure. Cores of more massive stars do contract, heat up and induce the next burning stage. Among the ashes of helium burning the nucleus with the smallest charge is ^{12}C . At densities of $\rho \approx 10^5 \text{ g cm}^{-3}$

and temperatures of $T \approx (6 - 8) \times 10^8$ K the Maxwell-Boltzmann velocity distribution reaches energies sufficient to penetrate the Coulomb barrier in the $^{12}\text{C}+^{12}\text{C}$ reaction, which has two open particle channels

$$^{12}\text{C} \left(\begin{array}{l} ^{12}\text{C}, \alpha \\ ^{12}\text{C}, p \end{array} \right) \begin{array}{l} ^{20}\text{Ne} \quad 4.62 \text{ MeV} \\ ^{23}\text{Na} \quad 2.24 \text{ MeV}. \end{array}$$

The products can interact with the released particles (protons and alphas)

$$^{23}\text{Na}(p, \alpha)^{20}\text{Ne} \quad ^{23}\text{Na}(p, \gamma)^{24}\text{Mg} \quad ^{12}\text{C}(\alpha, \gamma)^{16}\text{O}.$$

Besides these reactions, which dominate the energy generation, we also list in Table 5 the reactions whose fluxes are down by up to a factor of 100.

Table 5 Major Reactions in Carbon Burning

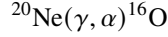
(a) basic energy generation
$^{12}\text{C}(^{12}\text{C}, \alpha)^{20}\text{Ne} \quad ^{12}\text{C}(^{12}\text{C}, p)^{23}\text{Na}$
$^{23}\text{Na}(p, \alpha)^{20}\text{Ne} \quad ^{23}\text{Na}(p, \gamma)^{24}\text{Mg} \quad ^{12}\text{C}(\alpha, \gamma)^{16}\text{O}$
(b) fluxes $> 10^2 \times$ (a)
$^{20}\text{Ne}(\alpha, \gamma)^{24}\text{Mg} \quad ^{23}\text{Na}(\alpha, p)^{26}\text{Mg}(p, \gamma)^{27}\text{Al}$
$^{20}\text{Ne}(n, \gamma)^{21}\text{Ne}(p, \gamma)^{22}\text{Na} (e^+ \nu)^{22}\text{Ne}(\alpha, n)^{25}\text{Mg}(n, \gamma)^{26}\text{Mg}$
$^{21}\text{Ne}(\alpha, n)^{24}\text{Mg} \quad ^{22}\text{Ne}(p, \gamma)^{23}\text{Na} \quad ^{25}\text{Mg}(p, \gamma)^{26}\text{Al}(e^+ \nu)^{26}\text{Mg}$
(c) low temperature, high density burning
$^{12}\text{C}(p, \gamma)^{13}\text{N}(e^+ \nu)^{13}\text{C}(\alpha, n)^{16}\text{O}(\alpha, \gamma)^{20}\text{Ne}$
$^{24}\text{Mg}(p, \gamma)^{25}\text{Al}(e^+ \nu)^{25}\text{Mg}$
$^{21}\text{Ne}(n, \gamma)^{22}\text{Ne}(n, \gamma)^{23}\text{Ne}(e^- \bar{\nu})^{23}\text{Na}(n, \gamma)^{24}\text{Na}(e^- \nu)^{24}\text{Mg} + s\text{-processing}$

The Q-value of the proton capture reaction on ^{12}C is 1.93MeV. Eq.(6), when utilizing the detailed balance relation between forward capture and reverse photodisintegration, results in the fact that the photodisintegration reactions are faster than the inverse capture reactions if $kT > 1/24Q$. This means that in high temperature carbon burning, close to $8 \times 10^8\text{K}$, the photodisintegration of ^{13}N will win over the β^+ -decay and the reaction sequence (c) in Table 5 will not be of any importance. However, in low temperature carbon burning the photodisintegration is slow, and we have the ^{13}C neutron source similar to hot helium burning, with the protons being supplied from the carbon fusion reaction. Only in this latter case an increase in the total neutron/proton ratio occurs, which can decrease Y_e down to 0.4975. For burning conditions with higher temperatures Y_e from helium burning remains unchanged.

Besides the uncertainties in the measurements of reactions overlapping with Table 4, one has to discuss the behavior of the dominant fusion reaction $^{12}\text{C}+^{12}\text{C}$ (see e.g. for early and recent investigations Rolfs and Rodney, 1988; Caughlan and Fowler, 1988; Tang and Ru, 2022; Heine et al, 2022; Monpriat et al, 2022).

Neon Burning

The most abundant nuclei after carbon burning are ^{16}O , ^{20}Ne , and ^{24}Mg . The reaction $^{16}\text{O}(\alpha, \gamma)^{20}\text{Ne}$ has a Q-value of only 4.73 MeV. The typical reaction Q-value for reactions among stable nuclei is about 8-12 MeV. This means, that in the temperature range of 1-2 MeV (following the relation $kT > 1/24Q$), alpha particles will be liberated by the photodisintegration of ^{20}Ne , and can be used to rearrange nuclei



The typical conditions for neon burning in stars are $T \approx (1.2 - 1.4) \times 10^9 \text{K}$ and $\rho \approx 10^6 \text{ g cm}^{-3}$. Stars in the mass range $8-10M_{\odot}$ appear to not reach this stage to burn Ne in a stable fashion, but their cores become degenerate and they contract to high densities at low temperatures. In that case the electron Fermi energies start to become important and electron captures start to occur. The electrons turn degenerate with a Fermi energy for the completely degenerate non-relativistic case and $n_e = (\rho N_A Y_e)^{2/3}$

$$E_F = \frac{\hbar^2}{2m_e} (3\pi^2)^{2/3} n_e^{2/3}$$

$$E_F(\rho Y_e = 10^7 \text{ g cm}^{-3}) = 0.75 \text{ MeV} \quad (20)$$

$$E_F(\rho Y_e = 10^9 \text{ g cm}^{-3}) = 4.7 \text{ MeV}.$$

That means that electron captures, which are energetically prohibited $e^- + (Z, A) \rightarrow (Z-1, A) + \nu$ with a negative negative Q-value, can become possible and lead to an enhanced “neutronization” of the astrophysical plasma, in addition to the role of beta decays and electron captures with positive Q-values. In degenerate Ne-O-Mg cores electron captures on ^{20}Ne and ^{24}Mg cause the loss of degeneracy pressure support and introduce a collapse rather than only a contraction, which shortens all further burning stages on a collapse time scale (for detailed discussions see [Kirsebom et al, 2019](#); [Leung et al, 2020](#)).

More massive stars pass through the main neon burning reactions, as discussed above. In addition, many other reactions can occur with fluxes much smaller than for those reactions that dominate the energy generation. We present a list in [Table 6](#). However, there is not any important change in Y_e for these massive stars. For an overview discussing experimental and theoretical evaluation of alpha-induced reactions from Ne and Mg to Ca see [Rauscher et al \(2000\)](#).

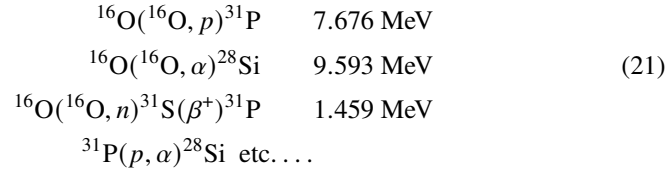
Oxygen Burning

The oxygen, produced in helium burning [$^4\text{He}(2\alpha, \gamma)^{12}\text{C}(\alpha, \gamma)^{16}\text{O}$], in carbon burning [$^{12}\text{C}(\alpha, \gamma)^{16}\text{O}$ with α 's from $^{12}\text{C}(^{12}\text{C}, \alpha)^{20}\text{Ne}$], and in neon burning

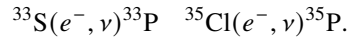
Table 6 Major Reactions in Neon Burning

(a) basic energy generation	
$^{20}\text{Ne}(\gamma, \alpha)^{16}\text{O}$	$^{20}\text{Ne}(\alpha, \gamma)^{24}\text{Mg}(\alpha, \gamma)^{28}\text{Si}$
(b) fluxes $> 10^2 \times$ (a)	
$^{23}\text{Na}(p, \alpha)^{20}\text{Ne}$	$^{23}\text{Na}(\alpha, p)^{26}\text{Mg}(\alpha, n)^{29}\text{Si}$
$^{20}\text{Ne}(n, \gamma)^{21}\text{Ne}(\alpha, n)^{24}\text{Mg}(n, \gamma)^{25}\text{Mg}(\alpha, n)^{28}\text{Si}$	
$^{28}\text{Si}(n, \gamma)^{29}\text{Si}(n, \gamma)^{30}\text{Si}$	
$^{24}\text{Mg}(\alpha, p)^{27}\text{Al}(\alpha, p)^{30}\text{Si}$	
$^{26}\text{Mg}(p, \gamma)^{27}\text{Al}(n, \gamma)^{28}\text{Al}(e^-, \bar{\nu})^{28}\text{Si}$	
(c) low temperature, high density burning	
$^{22}\text{Ne}(\alpha, n)^{25}\text{Mg}(n, \gamma)^{26}\text{Mg}(n, \gamma)^{27}\text{Mg}(e^-, \bar{\nu})^{27}\text{Al}$	
^{22}Ne left from prior neutron-rich carbon burning	

$[^{20}\text{Ne}(\gamma, \alpha)^{16}\text{O}]$, is still unburned and the nucleus with the smallest charge. At $\rho \approx 10^7 \text{ g cm}^{-3}$ and $T \approx (1.5 - 2.2) \times 10^9 \text{ K}$ the Coulomb barrier for oxygen fusion can be overcome, leading to the major reactions



In high density oxygen burning ($\rho > 2 \times 10^7 \text{ g cm}^{-3}$) two electron capture reactions become important and lead to a decrease in Y_e



Y_e can decrease to 0.495-0.4825. We list in Table 7 the major and minor reaction sequences. Many individual reactions of intermediate mass nuclei in oxygen and silicon burning have been analyzed in the past. Such experiments usually find quite good agreement with statistical model (Hauser-Feshbach) calculations, which will be discussed in the next section. Here we still want to point to the tremendous experimental efforts undertaken for determining solid cross section data.

Silicon Burning

When temperatures reach $(3 - 4) \times 10^9 \text{ K}$, every nucleus is connected to each other by reaction links which are open in both directions: (i) capture reactions due to high enough temperatures to overcome Coulomb barriers, (ii) photodisintegrations due to high enough temperatures and high energy photons in the Planck distribution. This situation, initiated by photodisintegration reactions on dominant ^{28}Si , which

Table 7 Major Reactions in Oxygen Burning

(a) basic energy generation	
$^{16}\text{O}(^{16}\text{O}, \alpha)^{28}\text{Si}$	$^{16}\text{O}(^{12}\text{O}, \text{p})^{31}\text{P}$
$^{16}\text{O}(^{16}\text{O}, \text{n})^{31}\text{S}(e^+ \nu)$	^{31}P
$^{31}\text{P}(\text{p}, \alpha)^{28}\text{Si}(\alpha, \gamma)^{32}\text{S}$	
$^{28}\text{Si}(\gamma, \alpha)^{24}\text{Mg}(\alpha, \text{p})^{27}\text{Al}(\alpha, \text{p})^{30}\text{Si}$	
$^{32}\text{S}(\text{n}, \gamma)^{33}\text{S}(\text{n}, \alpha)^{30}\text{Si}(\alpha, \gamma)^{34}\text{S}$	
$^{28}\text{Si}(\text{n}, \gamma)^{29}\text{Si}(\alpha, \text{n})^{32}\text{S}(\alpha, \text{p})^{35}\text{Cl}$	
$^{29}\text{Si}(\text{p}, \gamma)^{30}\text{P}(e^+ \nu)$	^{30}Si
electron captures	
$^{33}\text{S}(e^-, \nu)^{33}\text{P}(\text{p}, \text{n})^{33}\text{S}$	
$^{35}\text{Cl}(e^-, \nu)^{35}\text{S}(\text{p}, \text{n})^{35}\text{Cl}$	
(b) high temperature burning	
$^{32}\text{S}(\alpha, \gamma)^{36}\text{Ar}(\alpha, \text{p})^{39}\text{K}$	
$^{36}\text{Ar}(\text{n}, \gamma)^{37}\text{Ar}(e^+ \nu)$	^{37}Cl
$^{35}\text{Cl}(\gamma, \text{p})^{34}\text{S}(\alpha, \gamma)^{38}\text{Ar}(\text{p}, \gamma)^{39}\text{K}(\text{p}, \gamma)^{40}\text{Ca}$	
$^{35}\text{Cl}(e^-, \nu)^{35}\text{S}(\gamma, \text{p})^{34}\text{S}$	
$^{38}\text{Ar}(\alpha, \gamma)^{42}\text{Ca}(\alpha, \gamma)^{46}\text{Ti}$	
$^{42}\text{Ca}(\alpha, \text{p})^{45}\text{Sc}(\text{p}, \gamma)^{46}\text{Ti}$	
(c) low temperature, high density burning	
$^{31}\text{P}(e^- \nu)^{31}\text{S}$	$^{31}\text{P}(\text{n}, \gamma)^{32}\text{P}$
$^{32}\text{S}(e^-, \nu)^{32}\text{P}(\text{p}, \text{n})^{32}\text{S}$	
$^{33}\text{P}(\text{p}, \alpha)^{30}\text{Si}$	

produce protons, alpha-particles and neutrons, finally leads to an equilibrium where the abundances depend only on the nuclear mass (binding energy), density and temperature. Then the composition can be described by nuclear statistical equilibrium (NSE) and expressed by Eq.(22), which results from utilizing the chain of abundance ratios as given in Eq.(12) (an alternative derivation results from utilizing the chemical potentials of neutrons, protons and nucleus (Z, N) from a Maxwell-Boltzmann distribution and solving for the equation $Z\mu_p + N\mu_n = \mu_{Z,N}$).

$$Y_{Z,N} = G_{Z,N}(\rho N_A)^{A-1} \frac{A^{3/2}}{2^A} \left(\frac{2\pi\hbar^2}{m_u kT} \right)^{3/2(A-1)} \exp(B_{Z,N}/kT) Y_n^N Y_p^Z. \quad (22)$$

Electron captures, which occur on longer time scales than particle captures and photodisintegrations, are not in equilibrium and have to be followed explicitly. Thus, the NSE has to be solved for a given $\rho(t)$, $T(t)$, and $Y_e(t)$. This leads to two equations and a composition, resulting from Eq.(22) and a given Y_e , determined by

$$\begin{aligned} \sum_i A_i Y_i &= Y_n + Y_p + \sum_{Z,N} (Z + N) Y_{Z,N}(\rho, T, Y_n, Y_p) = 1 \\ \sum_i Z_i Y_i &= Y_p + \sum_{Z,N} Z Y_{Z,N}(\rho, T, Y_n, Y_p) = Y_e. \end{aligned} \quad (23)$$

In general, very high densities favor large nuclei, due to the high power of ρ^{A-1} , while very high temperatures favor light nuclei, due to $(kT)^{-3/2(A-1)}$. In the intermediate regime, occurring in hydrostatic stellar evolution, $\exp(E_B/kT)$ favors tightly bound nuclei with the highest binding energies in the mass range $A = 50 - 60$ (of the Fe-group), but depending upon the given Y_e . The width of the composition distribution is determined by the temperature. Y_e is determined by β^+ -decays and electron captures in Si-burning. Close to the end of core silicon burning, we have $Y_e \approx 0.46$.

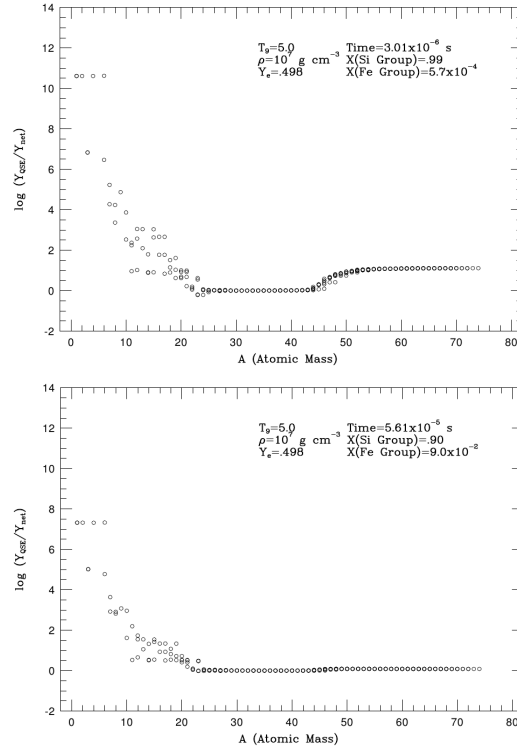
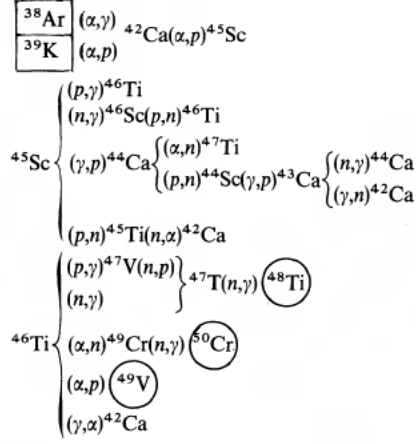


Fig. 1 Shown is the logarithmic ratio of equilibrium abundance predictions in comparison to results from full network calculations at two points in time when the mass fraction in the Si-group is still 99 and later 90%. Initially only the Si QSE-group is in full equilibrium ($=0$), while the light nuclei created in photodisintegration reactions and the heavier Fe-group nuclei created by capture reactions are still underabundant in comparison to equilibrium. However, we see constant lines for other QSE groups, i.e. the light group of n, p, ^4He and the Fe-group. The Fe group approaches equilibrium fast already when $X(\text{Si})=0.9$ while it will take a longer timescale by another order of magnitude until also the lighter nuclei have reached equilibrium. Image reproduced with permission from [Hix and Thielemann \(1996\)](#), copyright by AAS.

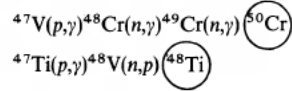
However, this final stage of Si-burning, resulting in a complete chemical equilibrium or NSE, is initially hampered by slow reactions, especially due to small

Q-values of reactions into closed neutron or protons shells. This leads initially to quasi-equilibrium groups (QSE), e.g. around ^{28}Si and a group centering on Fe or Ni nuclei, which are both within their groups in a complete equilibrium with abundance ratios as in Eq.(12), but the connections across the closed shells $N = Z = 20$ are hindered. Then the relative ratios of neighboring nuclei in each of the groups are in equilibrium, but the sum of abundances in each of the two groups is not identical to an NSE distribution. It is only approached by starting out with the QSE around Si dominating and, as a function of time, both - the Si and the Fe QSE groups - attain their final NSE values.

Basic reactions:



Additional reactions in high-temperature burning:



Important reactions in low-temperature burning:

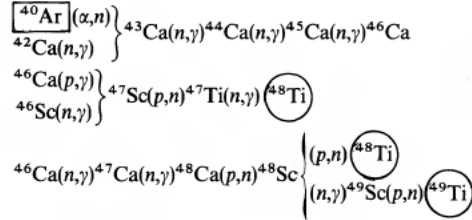


Fig. 2 The major reactions which connect the Si QSE-group and the Fe QSE-group during hydrostatic stellar Si-burning for $Y_e=0.498$ from an early analysis [Thielemann and Arnett \(1985\)](#). Dependent on the stellar mass this takes place for higher central temperatures (high mass stars) or slightly lower temperatures (massive stars in the lower mass interval $>10M_\odot$ which still experience central Si-burning). Members of the Si-group are indicated by a box, members of the Fe-group by a circle. Image reproduced with permission from [Thielemann and Arnett \(1985\)](#), copyright by AAS.

This behavior has been discussed in [Hix and Thielemann \(1996\)](#). Here we present a few illustrations clarifying this background. While temperatures of $T_9=5$ are in stellar evolution only reached at the end of Si-burning, we give here an example of a plasma consisting initially only of Si isotopes with a composition representing $Y_e=0.498$. We show the evolution at two points in time around 3×10^{-6} and 5.6×10^{-5} s.

Light particles are created by photodisintegration reactions on Si and heavier nuclei are produced by captures of these light particles. This means that initially these light particles and the heavier Fe-group are underabundant in comparison to a full NSE. This can be seen in the two panels of Fig.1.

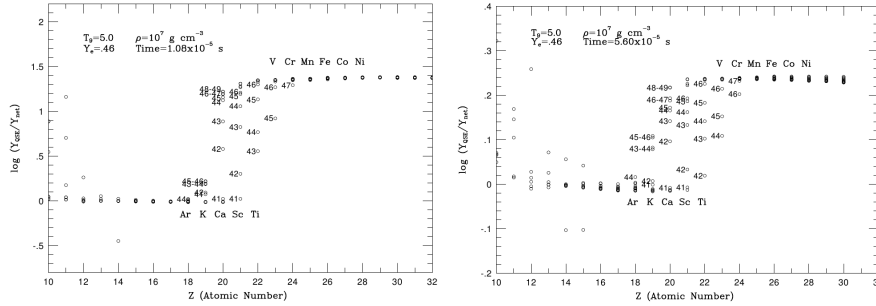


Fig. 3 The deviation from equilibrium decreases as a function of time, being already very close to equilibrium for $t \approx 5 \times 10^{-5}$ s. But it can be realized as well, that there exist still a (small) deviation between the two groups and that the nuclei out of equilibrium between the two groups vary as a function of time, increasing with Z (and being relatively neutron-rich for $Y_e=0.46$). In both cases nuclei close to the borders of the shell closures $N = Z = 20$ are the ones which still hinder to reach an equilibrium fast due to their slow reaction rates for reactions with small Q -values. Image reproduced with permission from [Hix and Thielemann \(1996\)](#), copyright by AAS.

[Thielemann and Arnett \(1985\)](#) made an early attempt for such Y_e -conditions to identify the important (slow) reactions which connect the two groups (see Fig.2). In a more extended study [Hix and Thielemann \(1996\)](#) analyzed the nuclei connecting the two QSE-groups. We can see the nuclei positioned between the two QSE-groups for two sets of conditions with $Y_e=0.46$, but at two points in time, close to $t \approx 1$ and 5×10^{-5} s. We notice that the deviation from equilibrium decreases as a function of time, being already very close to equilibrium in the latter case, but it can be realized as well, that there exist still a (small) deviation between the two groups and that the nuclei out of equilibrium between the two groups vary as a function of time, with increasing Z and are relatively neutron-rich for Y_e , see Fig.3.

Especially this last subsection, Si-burning, but also the previously discussed O-burning contain an overwhelming number of reactions of intermediate mass and heavy nuclei which need to be known and cannot all be provided by experiments. Thus, a reliable method for theoretical predictions is needed. The following section (after also going through explosive burning stages in the next subsection) will focus on the statistical model or Hauser-Feshbach approach, that can be applied if a sufficiently large density of excited state levels in the compound nucleus exists.

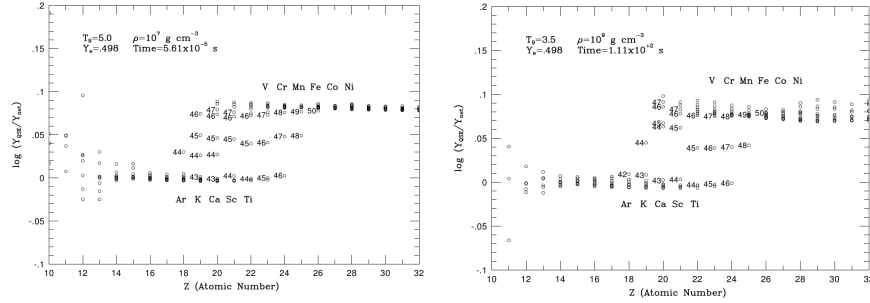


Fig. 4 Two results for $Y_e=0.498$ but at quite different temperatures and points in time. Similar deviations from equilibrium prevail for $t \approx 5 \times 10^{-6}$ s and in contrast for 111s. In both cases finally an NSE will be reached, but either for conditions close to explosive Si-burning or otherwise for conditions which are similar to the initial ignition conditions of hydrostatic Si-burning in massive stars. Image reproduced with permission from [Hix and Thielemann \(1996\)](#), copyright by AAS.

Nuclear burning in explosive environments

Many of the hydrostatic burning processes discussed in earlier subsections can occur also under explosive conditions at much higher temperatures and on shorter timescales. The major reactions remain still the same in many cases, but often the beta-decay half-lives of unstable products are longer than the timescales of the explosive processes under investigation. This requires in general the additional knowledge of nuclear cross sections for unstable nuclei. (For the further influence of weak interactions in hydrostatic and explosive burning see [Langanke et al \(2021\)](#) and the chapter by Famiano et al.).

Extensive calculations of explosive carbon, neon, oxygen, and silicon burning, appropriate for supernova explosions, have already been performed in the late 60s and early 70s with the accuracies possible in those days, before detailed stellar modeling became available (for present-day results see e.g. [Curtis et al, 2019](#), and the chapters by Seitenzahl & Pakmor, C. Fröhlich, S. Wanajo, M. Obergaulinger, and A. Bauswein & H.-T. Janka). Besides minor additions of ^{22}Ne after He-burning (or nuclei which originate from it in later burning stages), the fuels for explosive nucleosynthesis consist mainly of alpha-particle nuclei like ^{12}C , ^{16}O , ^{20}Ne , ^{24}Mg , or ^{28}Si . Because the timescale of explosive processing is very short (a fraction of a second to several seconds), only few beta-decays can occur during explosive nucleosynthesis events (unless highly unstable species are produced), resulting in heavier nuclei, again with $N \approx Z$. However, a spread of nuclei around a line of $N=Z$ is involved and many reaction rates for unstable nuclei have to be known. Dependent on the temperature, explosive burning produces intermediate to heavy nuclei.

Two processes encounter nuclei far from stability where either a large supply of neutrons or protons is available. In those cases, the r-process and the rp-process (i.e. explosive hydrogen burning), nuclei close to the neutron and proton drip lines can be produced and beta-decay timescales can be short in comparison to the process

timescales. We will not discuss these nucleosynthesis processes in detail here, but refer to the chapters by M. Wiescher and M. Pfützner & C. Mazzocchi for reactions involving proton-rich nuclei and the chapters by S. Goriely and S. Nishimura for reactions involving neutron-rich nuclei in r-process environments. Independent of these individual aspects, for all the intermediate and heavy nuclei we will present (after a short discussion of these explosive nucleosynthesis environment) theoretical methods to determine nuclear reaction cross sections and reaction rates.

While most of the explosive burning processes are to some extent (with the exceptions mentioned above and below) "cousins" of their hydrostatic versions, involving just much shorter timescales and a more extended set of nuclei, this is different for Si-burning which we will discuss in a separate subsection. A possible connection between explosive Si-burning and the beginning of an r-process is pointed out as well.

Burning timescales for explosive He, C, Ne, O, and Si-burning

In stellar evolution, burning timescales are dictated by the energy loss timescales of stellar environments. Processes like hydrogen and helium burning, where the stellar energy loss is dominated by the photon luminosity, choose temperatures with energy generation rates equal to the radiation losses. For the later burning stages neutrino losses play the dominant role among cooling processes and the burning timescales are determined by temperatures where neutrino losses are equal to the energy generation rate. These criteria led to the narrow bands in temperatures and densities discussed in previous subsections on hydrostatic burning stages in stellar evolution.

Explosive events are determined by hydrodynamic equations which provide different temperatures or timescales for the burning of available fuel. We can generalize the question by defining a burning timescale, dependent on whether the key reaction is a fusion reaction or a photodisintegration, responsible for the destruction of the major fuel nuclei i

$$\tau_i = \left| \frac{Y_i}{\dot{Y}_i} \right| = \frac{1}{\rho N_A \langle \sigma v \rangle (T) Y_{fuel}} \quad (24)$$

$$\text{or} = \frac{1}{\lambda_\gamma(T)}$$

These timescales for the fuels $i \in \text{H, He, C, and O}$ are determined by the major fusion destruction reaction. They are in all cases temperature dependent and for a fusion process they are also density dependent. Ne- and Si-burning, which are dominated by (γ, α) destruction of ^{20}Ne and ^{28}Si , have timescales only determined by the burning temperatures. The temperature dependencies are typically exponential, due to the functional form of the corresponding $N_A \langle \sigma v \rangle$. The density dependencies are linear for fusion reactions, as seen from Eq.(10), with the exception of

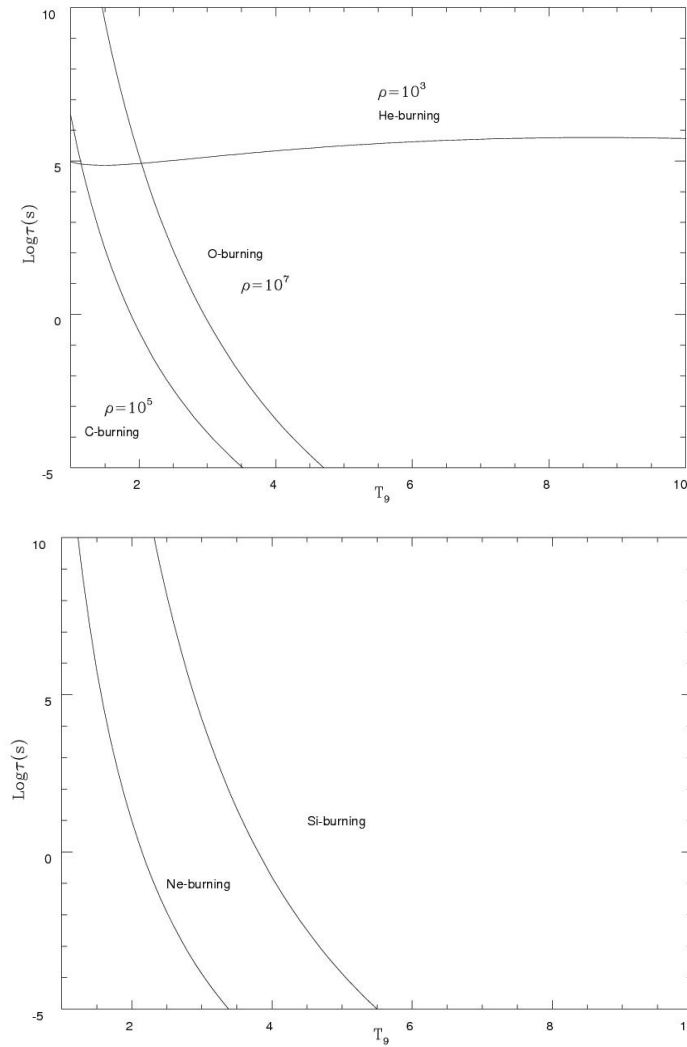


Fig. 5 Burning time scales for fuel destruction of He-, C-, Ne-, O-, and Si-burning as a function of temperature, as defined in Eq.(24) and generalized to photodisintegrations and three-body reactions, accordingly. A 100 fuel mass fraction was assumed. When rewriting Eq.(24) for ${}^4\text{He}$, the destruction of three identical particles has to be considered. The density-dependent burning time scales are labeled with the chosen typical density. They scale linearly for C- and O-burning and quadratically for He-burning. Notice that the almost constant He-burning time scale beyond $T_9=1$ has the effect that efficient destruction on explosive time scales can only be attained for high densities. Image reproduced with permission from Thielemann et al (2018), copyright by Springer Nature.

He-burning. We have plotted these burning timescales as a function of temperature (see Fig.5), assuming a fuel mass fraction of 1. The curves for (also) density dependent burning processes are labeled with a typical density. He-burning has a quadratic density dependence, C- and O-burning depend linearly on density. If we take typical explosive burning timescales to be of the order of seconds (e.g. in supernovae), we see that one requires temperatures to burn essential parts of the fuel in excess of 4×10^9 K (Si-burning), 3.3×10^9 K (O-burning), 2.1×10^9 K (Ne-burning), and 1.9×10^9 K (C-burning). Beyond 10^9 K He-burning is determined by an almost constant burning time scale. We see that essential destruction on a time scale of 1s is only possible for densities $\rho > 10^5 \text{ g cm}^{-3}$. This is usually not encountered in He-shells of massive stars.

Special features of explosive Si-burning

Zones which experience temperatures in excess of $4.0\text{--}5.0 \times 10^9$ K undergo explosive Si-burning. For $T > 5 \times 10^9$ K essentially all Coulomb barriers can be overcome and a nuclear statistical equilibrium is established. Such temperatures lead to complete Si-exhaustion and produce Fe-group nuclei. The doubly-magic nucleus ^{56}Ni , with the largest binding energy per nucleon for $N=Z$, is formed with a dominant abundance in the Fe-group in case Y_e is larger than 0.49. Explosive Si-burning can be divided into three different regimes: (i) incomplete Si-burning and complete Si-burning with either a (ii) normal or an (iii) alpha-rich freeze-out. Which of the three regimes is encountered depends on the peak temperatures and densities attained during the passage of supernova shock front (see Fig.20 in Woosley et al, 1973, and Fig.6 for applications to supernova calculations). One recognizes that SNe Ia and SN II (core-collapse supernovae) experience different regions of complete Si-burning.

The most abundant nucleus in the normal and alpha-rich freeze-out is ^{56}Ni , in case the neutron excess is small, i.e., Y_e is larger than 0.49. It is evident that the electron fraction Y_e has a major imprint on the final composition. Nuclei with a Z/A -value corresponding to the global Y_e show the largest abundances, combined with a maximum in binding energy. The even-Z-even-N nuclei show the largest abundances due to their large binding energies. In an alpha-rich freeze-out final alpha-captures (or rather the shift of the upper QSE-group to heavier nuclei, based on the large ^4He abundance) play a dominant role for the less abundant nuclei, transforming e.g. ^{56}Ni , ^{57}Ni , and ^{58}Ni into ^{60}Zn , ^{61}Zn , and ^{62}Zn and leaving trace abundances of ^{32}S , ^{36}Ar , ^{40}Ca , ^{44}Ti , ^{48}Cr , ^{52}Fe , ^{54}Fe , and ^{55}Co . In that case the major NSE nuclei ^{56}Ni , ^{57}Ni , and ^{58}Ni get depleted when the remaining alpha fraction increases, while all other species mentioned above increase. At high temperatures in complete Si-burning, before freeze-out or in a normal freeze-out, the abundances are in a full NSE. An alpha-rich freeze-out occurs generally at low densities when the triple-alpha reaction, transforming ^4He into ^{12}C , is not fast enough to keep the He-abundance in equilibrium during the fast expansion and cooling in explosive events (see Fig.6).

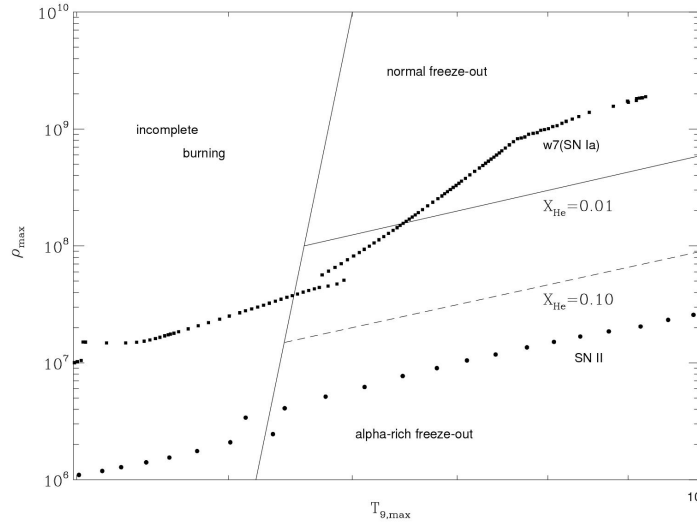


Fig. 6 Division of the $\rho_p - T_p$ -plane into incomplete and complete Si-burning with normal and alpha-rich freeze-out. Contour lines of constant ${}^4\text{He}$ mass fractions in complete burning are given for levels of 1 and 10%. They coincide with lines of constant radiation entropy per gram of matter. For comparison also the maximum $\rho - T$ -conditions for individual mass zones of type Ia and type II (core-collapse) supernovae are indicated. Image reproduced with permission from [Thielemann et al \(2018\)](#), copyright by Springer Nature.

This also leads to a slow supply of carbon nuclei still during freeze-out, leaving traces of alpha nuclei, which did not fully make their way up to ${}^{56}\text{Ni}$.

Incomplete Si-burning is characterized by peak temperatures of $4 - 5 \times 10^9 \text{K}$. Temperatures are not high enough for an efficient bridging of the bottle neck above the proton magic number $Z=20$ by nuclear reactions. Besides the dominant fuel nuclei ${}^{28}\text{Si}$ and ${}^{32}\text{S}$, we find the alpha-nuclei ${}^{36}\text{Ar}$ and ${}^{40}\text{Ca}$ being most abundant. Partial leakage through the bottle neck above $Z=20$ produces ${}^{56}\text{Ni}$ and ${}^{54}\text{Fe}$ as dominant abundances in the Fe-group. Smaller amounts of ${}^{52}\text{Fe}$, ${}^{58}\text{Ni}$, ${}^{55}\text{Co}$, and ${}^{57}\text{Ni}$ are encountered. In a superposition of (a) incomplete Si-burning, (b) complete Si-burning with alpha-rich freeze-out, and (c) explosive O-burning supernova explosions can provide good fits to solar abundances. For recent features of the results of explosive burning in core-collapse supernovae see e.g. [Curtis et al \(2019\)](#); [Ghosh et al \(2022\)](#) and in type Ia supernovae see e.g. [Lach et al \(2020\)](#); [Leung and Nomoto \(2021\)](#).

The r-process

The operation of an r-process is characterized by the fact that 10 to 100 neutrons per seed nucleus in the Fe-peak (or beyond in an alpha-rich freeze-out) have to be

available to form all heavier r-process nuclei by neutron capture. This translates into a $Y_e=0.15-0.3$. Such a high neutron excess can only be obtained through capture of energetic electrons (on protons or nuclei) which have to overcome large negative Q-values. This can be achieved by degenerate electrons with large Fermi energies and requires a compression to densities of $10^{11} - 10^{12} \text{g cm}^{-3}$, with a beta equilibrium between electron captures and β^- -decays as found in supernova core collapse and the forming neutron stars.

Another option is an extremely alpha-rich freeze-out in complete Si-burning with moderate and Y_e 's (even >0.42). After the freeze-out of charged particle reactions in matter which expands from high temperatures but relatively low densities, 70, 80, 90 or 95% of all matter can be locked into ^4He with $N=Z$. Figure 6 showed the onset of such an extremely alpha-rich freeze-out by indicating contour lines for He mass fractions of 1 and 10%. These contour lines correspond to $T_9^3/\rho=\text{const}$, which is proportional to the entropy per gram of matter of a radiation dominated gas. Thus, the radiation entropy per gram of baryons can be used as a measure of the remaining He mass-fraction. In such high entropy conditions all excess neutrons are left with the remaining mass fraction of Fe-group (or heavier) nuclei and neutron captures can proceed to form the heaviest r-process nuclei. A recent general review of the functioning of an r-process, the nuclear physics input, astrophysical sites and related observations can be found in [Cowan et al \(2021\)](#).

Explosive H-burning and proton-rich nuclei

We will not discuss here in detail explosive hydrogen burning which takes place in novae and X-ray bursts, as their nucleosynthesis contribution to our known abundance pattern is not significant, however contributions to ^7Li , ^{15}N , and ^{17}O , ^{22}Na , ^{26}Al are reported (see e.g. [Cescutti and Molaro, 2019](#); [Vasini et al, 2022, 2023](#)). Novae, due to high temperatures attained in H-burning, burn H in the accreted material not via the well-known CNO-cycle, but in the so-called hot CNO cycle. It is characterized by the fact that in the branching between the slow beta-decay of ^{13}N and a further proton capture to ^{14}O , the proton capture wins because of a highly enhanced reaction rate for such conditions. In a similar way hot CNO-type cycles for elements beyond Ne re-arrange nuclei up to Mg and Si. When including ejecta of such nova explosions, a few not highly abundant isotopes up to Mg and Si can be considered to have a non-negligible contribution from novae ([Jose, 2016](#)).

In type I X-ray bursts, due to the explosive ignition of H- and subsequent He-burning reactions, matter from the hot CNO cycle can even be transferred to heavier nuclei up to ^{100}Sn via the rp-process. This is an important stellar explosion, observed in X-rays, but the explosion energy is likely not sufficient to eject matter out of the high gravitational binding of the neutron star. A detailed discussion of novae and X-ray bursts can be found in [Jose \(2016\)](#), the evolution of knowledge on the nuclear reactions evolved over many years from [Wiescher et al \(1986\)](#) over [Schatz et al \(1998\)](#) to [Cyburt et al \(2010\)](#); [Schatz and Ong \(2017\)](#); [Meisel et al \(2020\)](#).

In addition to the above mentioned explosive burning processes, there exist other processes producing some isotopes beyond iron that are not accessible by neutron capture processes. They include the p-process or γ -process (occurring as a byproduct of explosive Ne-burning which was discussed before) and the νp -process (Fig. 7), responsible for proton-rich stable nuclei up to $A = 80$ – 90 . The p-process consist mainly of photo dissociation of existing heavy isotopes. This moves matter from nuclei previously produced by the s- and r-process to the proton-rich side of stability. The initial suggestion was that conditions in a hydrodynamic shock wave triggers this process when running through layers of an exploding star that contain already heavy nuclei from previous generations. For an overview of possible sources for p-rich nuclei and the relevant nuclear physics, see [Rauscher et al \(2013\)](#); [Roberti et al \(2023\)](#).

An additional option to produce light p-nuclei is the so-called νp -process in proton-rich ejecta in supernova explosions ([Fröhlich et al, 2006](#); [Wanajo et al, 2011](#); [Ghosh et al, 2022](#)).

What type of reactions are needed in explosive burning?

After going through the various hydrostatic and explosive burning processes which need input for nuclear reaction cross sections, we attempt to give a short overview on the regions in the nuclear chart where such reaction cross sections and reaction rates are needed. A summary of all these processes and their actions in specific regions of the nuclear chart is given in Fig.7. These include proton capture reaction in the rp-process and νp -process, photodisintegration reactions in the p- or γ -process, and neutron capture reactions in the r-process. The other explosive burning processes mentioned in the previous subsections work closer to stability, but also include to some extent unstable nuclei, for which charged particle and neutron capture reactions need to be predicted.

Thermonuclear Rates and the Hauser-Feshbach Formlism

In the section on hydrostatic burning stages, we indicated that at least all the early burning stages rely on experimentally determined nuclear reaction cross sections. In late burning stages and explosive burning a number of unstable nuclei are produced and a much larger amount of stable nuclei. It is thus advisable to look into specific experimental techniques or alternatively into reliable theoretical approaches which can provide the necessary information. Explosive burning in supernovae involves in general intermediate mass and heavy nuclei. Due to a large nucleon number they have intrinsically a high density of excited states. A high level density in the compound nucleus at the appropriate excitation energy allows to make use of the statistical model approach for compound nuclear reactions (Hauser-Feshbach), which averages

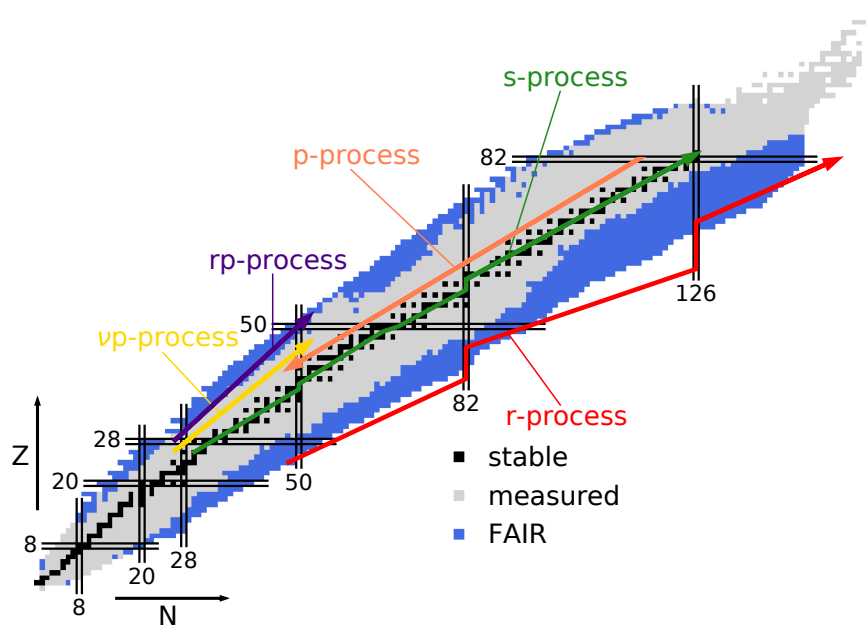


Fig. 7 (courtesy of M. Jacobi and A. Arcones) The nuclear chart with stable isotopes marked with black boxes, the gray region indicates nuclei that have been produced already in the laboratory, and the light blue region shows the exotic isotopes that rare isotope facilities will discover. The various explosive nucleosynthesis processes discussed in previous subsections are schematically indicated by color lines. Explosive C, Ne, O, and Si burning (unless happening under very neutron-rich conditions) involve stable and unstable nuclei close to stability. The s-process, taking place in hydrostatic He-burning, is also shown here, but it can to a large extent (with exceptions) be investigated with experimentally determined neutron capture cross sections of stable nuclei.

over resonances. Therefore, it is often colloquially termed that the statistical model is only applicable for intermediate and heavy nuclei, which gives repeatedly rise to misunderstandings. The only necessary condition for application of the statistical model formalism is a large number of resonances at the appropriate bombarding energies, so that the cross section can be described by average transmission coefficients. Whether we have a light or heavy nucleus is only of secondary importance. A high level density automatically implies that the nucleus can equilibrate in the classical compound nucleus picture.

As the capture of an alpha particle leads usually to larger Q-values than neutron or proton captures, the compound nucleus is created at a higher excitation energy and especially in the case of alpha captures it is often even possible to apply the Hauser-Feshbach formalism for nuclei as light as Li. Another advantage of alpha capture is that the capture Q-values vary very little with the N/Z-ratio of a nucleus. This means that the requirements are equally well fulfilled near stability as at the proton or neutron drip lines, which makes the application very safe for all intermediate and

heavy nuclei (and for light nuclei the level density test has to be done individually). Opposite to the behavior for alpha-induced reactions, the reaction Q-values for proton or neutron captures vary strongly with the N/Z-ratio, leading eventually to vanishing Q-values at the proton or neutron drip line. For small Q-values the compound nucleus is created at low excitation energies and also for intermediate nuclei the level density can be quite small. Therefore, it is not advisable to apply the statistical model approach close to the proton drip line for intermediate nuclei. For neutron captures close to the neutron drip line in r-process applications it might be still permissible for heavy and often deformed nuclei, which have a high level density already at very low excitation energies. On the other hand, this method is not applicable for neutron-rich light nuclei. Where predictions for nuclear reaction rates are needed to perform investigations in the related astrophysical processes has been outlined in Fig.7.

The statistical model approach has been employed in the calculation of thermonuclear reaction rates for astrophysical purposes by many researchers, starting with [Truran et al \(1966\)](#), who only made use of ground state properties. [Arnould \(1972\)](#) pointed out the importance of excited states. Extended compilations have been provided ([Holmes et al, 1976](#); [Woosley et al, 1978](#); [Thielemann et al, 1986](#); [Rauscher and Thielemann, 2000](#); [Goriely et al, 2008](#), for updates see ⁴). The codes for the latter three entries are known under the names SMOKER, NON-SMOKER, and TALYS. More recently, the code SMARAGD ([Rauscher, 2010, 2011](#)) has been developed as a successor to NON-SMOKER, with improvements in the treatment of charged particle and photon transmissions, in the nuclear level density, and with inclusion of recent experimental information on low-lying excited states. Reaction rate compilations obtained from calculations using NON-SMOKER and TALYS are presently the ones utilized in large scale applications in all subfields of nuclear astrophysics, when experimental information is unavailable. SMARAGD is being used to analyze experimental data and for improvements of smaller sets of reaction rates ([Cyburt et al, 2010](#)) but a large-scale set of reaction rates has not been published yet.

A high level density in the compound nucleus permits to use averaged transmission coefficients T , which do not reflect a resonance behavior, but rather describe absorption via an imaginary part in the (optical) nucleon-nucleus potential (for details see, e.g. [Mahaux and Weidenmuller, 1979](#)). This leads to the well known expression

$$\sigma_i^{\mu\nu}(j, o; E_{ij}) = \frac{\pi\hbar^2/(2\mu_{ij}E_{ij})}{(2J_i^\mu + 1)(2J_j + 1)} \quad (25)$$

$$\times \sum_{J, \pi} (2J + 1) \frac{T_j^\mu(E, J, \pi, E_i^\mu, J_i^\mu, \pi_i^\mu) T_o^\nu(E, J, \pi, E_m^\nu, J_m^\nu, \pi_m^\nu)}{T_{tot}(E, J, \pi)}$$

⁴ <https://nucastro.org>, <https://reaclib.jinaweb.org> and <https://www-nds.iaea.org>, including TALYS results

for the reaction $i^\mu(j, o)m^\nu$ from the target state i^μ to the excited state m^ν of the final nucleus, with center of mass energy E_{ij} and reduced mass μ_{ij} . J denotes the spin, E the excitation energy, and π the parity of excited states. When these properties are used without subscripts they describe the compound nucleus, subscripts refer to the participating nuclei in the reaction $i^\mu(j, o)m^\nu$ and superscripts indicate the specific excited states. Experiments measure $\sum_\nu \sigma_i^{0\nu}(j, o; E_{ij})$, summed over all excited states of the final nucleus, with the target in the ground state. Target states μ in an astrophysical plasma are thermally populated and the astrophysical cross section $\sigma_i^*(j, o)$ is given by

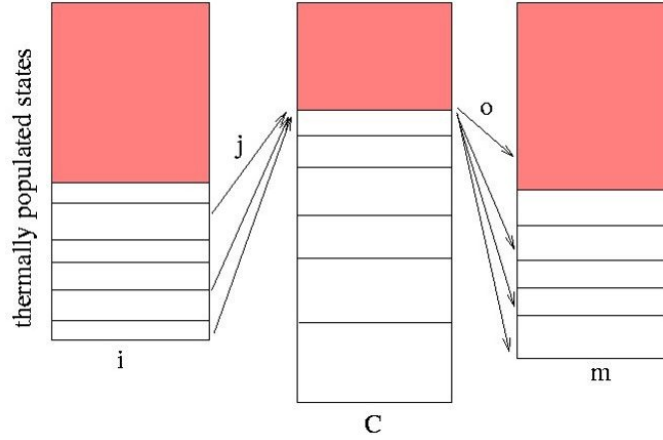


Fig. 8 Energetics for the reaction $i(j, o)m$ and its inverse $m(o, j)i$ for transitions through a resonance state (E, J^π) in the compound nucleus C .

$$\sigma_i^*(j, o; E_{ij}) = \frac{\sum_\mu (2J_i^\mu + 1) \exp(-E_i^\mu/kT) \sum_\nu \sigma_i^{\mu\nu}(j, o; E_{ij})}{\sum_\mu (2J_i^\mu + 1) \exp(-E_i^\mu/kT)}. \quad (26)$$

The summation over ν replaces $T_o^\nu(E, J, \pi)$ in Eq.(25) by the total transmission coefficient

$$T_o(E, J, \pi) = \sum_{\nu=0}^{\nu_m} T_{om}^\nu(E, J, \pi, E_m^\nu, J_m^\nu, \pi_m^\nu) + \int_{E_m^{\nu_m}}^{E-S_{m,o}} \sum_{J_m, \pi_m} T_{om}(E, J, \pi, E_m, J_m, \pi_m) \rho(E_m, J_m, \pi_m) dE_m. \quad (27)$$

Here $S_{m,o}$ is the channel separation energy, and the summation over excited states above the highest experimentally known state ν_m is changed to an integration over the

level density ρ . The summation over target states μ in Eq.(26) has to be generalized accordingly.

The important ingredients of statistical model calculations are the particle and γ -transmission coefficients T and the level density of excited states ρ . Therefore, the reliability of the of such calculations is determined by the accuracy with which these components can be evaluated. In the following we want to discuss the methods utilized to estimate these quantities and recent improvements.

Particle Transmission Coefficients

The transition from an excited state in the compound nucleus (E, J, π) to the state $(E_i^\mu, J_i^\mu, \pi_i^\mu)$ in nucleus i via the emission of a particle j is given by a summation over all quantum mechanically allowed partial waves

$$T_j^\mu(E, J, \pi, E_i^\mu, J_i^\mu, \pi_i^\mu) = \sum_{l=|J-s|}^{J+s} \sum_{s=|J_i^\mu-J_j|}^{J_i^\mu+J_j} T_{jis}(E_{ij}^\mu). \quad (28)$$

Here the angular momentum \vec{l} and the channel spin $\vec{s} = \vec{J}_j + \vec{J}_i^\mu$ couple to $\vec{J} = \vec{l} + \vec{s}$. The individual transmission coefficients T_l are calculated by solving the Schrödinger equation with an optical potential for the particle-nucleus interaction. While all early studies of thermonuclear reaction rates (Truran et al, 1966; Arnould, 1972; Holmes et al, 1976; Woosley et al, 1978) employed optical square well potentials and made use of the black nucleus approximation, the other compilations utilize optical potentials from microscopic calculations. The resulting s-wave neutron strength function (the average ratio of the width of states populated by s-wave neutrons and the appropriate level spacing D for a 1 eV capture energy) can be expressed by $S_0 = \langle \Gamma^o/D \rangle_{1\text{eV}} = (1/2\pi)T_{n(l=0)}(1\text{eV})$. A specific optical potential choice (Jeukenne et al, 1977) with corrections for the imaginary part and updated parameters for low energies (Lejeune, 1980) is shown in Fig.9 (utilized in the NON-SMOKER code).

In a similar way there exist a variety of optical potentials for protons (including Jeukenne et al, 1977, with the appropriate energetics, see also many more options in the TALYS package). Alpha particles have been treated in many cases with a phenomenological Woods-Saxon potential based on extensive data by McFadden and Satchler (McFadden and Satchler, 1966). In general, for alpha particles and heavier projectiles, the best results can probably be obtained with folding potentials (see e.g. Satchler and Love, 1979; Mohr et al, 2020).

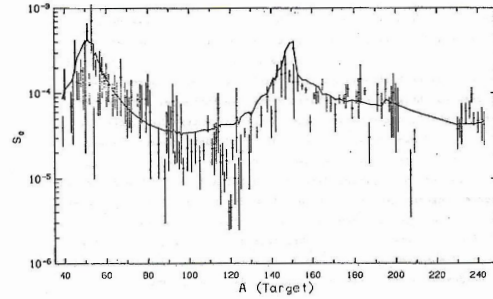


Fig. 9 Neutron strength function when utilizing a sophisticated optical potential (Jeukenne et al, 1977). An equivalent square well potential would result in a straight line. When utilizing a spherical potential a deviation from experiment around $A=160$ would show up, with an S_0 -line similar to a sinus curve. This is avoided here by treating deformed nuclei in a very simplified way (without utilizing more sophisticated coupled channel calculations) by using an effective spherical potential of equal volume, based on averaging the deformed potential over all possible angles between the incoming particle and the orientation of the deformed nucleus. Image reproduced with permission from Cowan et al (1991), copyright by Elsevier.

γ -Transmission Coefficients

At low energies photon captures on nuclei lead to relatively simple excited states, often involving only few particles in the nucleus. Beyond about 10 MeV so-called giant resonances are populated which correspond to a collective motion involving many if not all particles of a nucleus. They occur as electric or magnetic multipole resonances and can be excited by capture of a photon or can decay by emitting a photon. The dipole E1 and M1 resonances dominate. In a macroscopic way they can be understood by protons oscillating against neutrons (a) in the Goldhaber-Teller mode where fixed proton and neutron density distributions move against each other or (b) in the Steinwedel-Jensen mode with density oscillations of neutrons against protons taking place within a fixed nuclear surface. In such "macroscopic" descriptions the resonance energy and its width can be explained with the ingredients of macroscopic-microscopic nuclear mass models (e.g. Thielemann et al, 1986; Thielemann and Arnould, 1983; Rauscher and Thielemann, 2000). Extended collections of experimental data, showing essentially a Lorentzian distribution as a function of energy, have been provided in the past (e.g. Berman and Fultz, 1975; Junghans et al, 2008), see for recent comprehensive reviews (Ishkhanov and Kapitonov, 2021; Liang and Litvinova, 2022), the latter reference corresponding to the chapter by Liang & Litvinova in this Handbook, containing a detailed derivation within a microscopic (rather than phenomenological "macroscopic") description of these giant resonances. Both types of options to choose are available in the TALYS code. In the more phenomenological approach the E1 transitions are calculated on the basis of the Lorentzian representation of the Giant Dipole Resonance (GDR). Within this

model, the E1 transmission coefficient for the transition emitting a photon of energy E_γ in a nucleus ${}^A_Z X$ is given by

$$T_{E1}(E_\gamma) = \frac{8}{3} \frac{NZ}{A} \frac{e^2}{\hbar c} \frac{1 + \chi}{mc^2} \sum_{i=1}^2 \frac{i}{3} \frac{\Gamma_{G,i}^2 E_\gamma^4}{(E_\gamma^2 - E_{G,i}^2)^2 + \Gamma_{G,i}^2 E_\gamma^2}. \quad (29)$$

Here $\chi (= 0.2)$ accounts for the neutron-proton exchange contribution and the summation over i includes two terms which correspond to the split of the GDR in statically deformed nuclei, with oscillations along ($i=1$) and perpendicular ($i=2$) to the axis of rotational symmetry. Specific experimental results (Junghans et al, 2008) are shown in Fig.10.

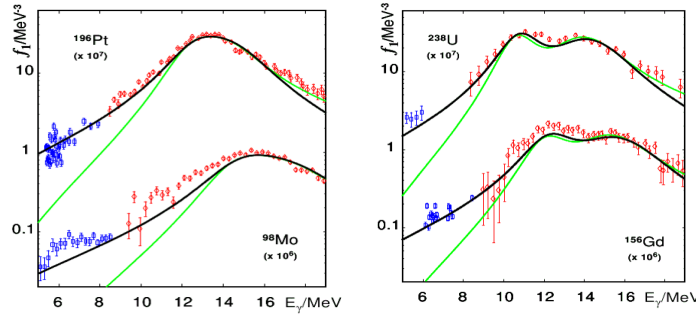


Fig. 10 Experimental strength functions of the Giant Dipole Resonance $f_{E1}(E_\gamma) = (T_{E1}(E_\gamma)/2\pi)(E_\gamma)^{-3}$ for spherical and deformed nuclei from Junghans et al (1998). For deformed nuclei the Lorentzian form splits into two sub-resonances (see text). The lines represent two choices for the description of the GDR width chosen by Junghans et al (2008). This includes, however, also low-lying E1 strength, which will be discussed below in more detail. Image reproduced with permission from Junghans et al (2008), copyright by Elsevier.

As discussed above, the GDR resonance energy E_G can be predicted within macroscopic (hydrodynamic) approaches based on the ingredients of macroscopic-microscopic mass models (Thielemann and Arnould, 1983; Rauscher and Thielemann, 2000), which gives excellent fits to the GDR energies and can also predict the split of the resonance for deformed nuclei, when making use of the deformation. In that case, the two resonance energies are related to the mean value by the following expression (Danos, 1958)

$$\begin{aligned} E_{G,1} + 2E_{G,2} &= 3E_G \\ E_{G,2}/E_{G,1} &= 0.911\eta + 0.089. \end{aligned} \quad (30)$$

η is the ratio of (1) the diameter along the nuclear symmetry axis and (2) the diameter perpendicular to it. It can be obtained from the experimentally known deformation or mass model predictions (see Fig.11).

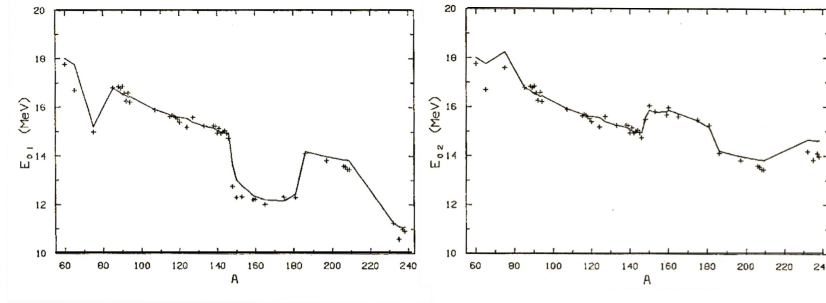


Fig. 11 E1 giant dipole resonance energy for oscillations parallel (E_{01}) and perpendicular (E_{02}) to the rotational symmetry of deformed nuclei. For spherical nuclei both energies coincide. The energies are predicted with parameters from microscopic-macroscopic mass models (as utilized in the NON-SMOKER code), deformations taken from experiments or mass models as well. Image reproduced with permission from [Cowan et al \(1991\)](#), copyright by Elsevier

The width of the GDR Γ_G is less understood, but can also be predicted in a phenomenological approach via the ingredients of macroscopic-microscopic nuclear mass models which satisfactorily reproduces the experimental data for spherical and deformed nuclei. The GDR width can be described as a superposition of a macroscopic width due to the viscosity of the nuclear fluid and a coupling to quadrupole surface vibrations of the nucleus ([Thielemann and Arnould, 1983](#); [Rauscher and Thielemann, 2000](#); [Goriely, 1998](#)). The width is reduced near magic nuclei, because these closed shell nuclei act within the hydrodynamic picture in a stiff way and couple less to the quadrupole surface vibrations. Alternatively microscopic approaches have been utilized within the quasi-particle Random Phase Approximation (QRPA) (see e.g., besides a macroscopic approach similar to the above description, different options in the TALYS code based on Skyrme Hartree-Fock BCS, Skyrme Hartree-Fock-Bogoluibov, the temperature-dependent relativistic mean field or the Gogny Hartree-Fock-Bogoluibov model) or also the Relativistic Quasiparticle Time Blocking approximation (RQTBA) framework ([Litvinova et al, 2009](#)). For a general review see [Liang and Litvinova \(2022\)](#).

The total radiation width at the neutron separation energy for nuclei in experimental compilations can be calculated via the total photon transmission coefficients for E1 radiation from a compound nucleus state with energy E , spin J , and parity π is given by

$$T_\gamma(E, J, \pi) = \sum_{\nu=0}^{\nu_C} T_\gamma^\nu(E, J, \pi, E_C^\nu, J_C^\nu, \pi_C^\nu) + \int_{E_m^{\nu_C}}^E \sum_{J_C, \pi_C} T_\gamma(E, J, \pi, E_C, J_C, \pi_C) \rho(E_C, J_C, \pi_C) dE_C, \quad (31)$$

where the first term represents a summation over the known low-lying states ν up to an excitation energy $E_\omega = E_C^\nu$, while an integration involving the level density ρ is performed at higher excitation. $T_\gamma^\nu(E, J, \pi, E_C^\nu, J_C^\nu, \pi_C^\nu)$ is either zero if the E1 selection rules are violated, or equal to $T_{E1}(E_\gamma = E - E_C^\nu)$ otherwise. With T_{E1} from Eq.(29) the average radiation width $\langle \Gamma_\gamma(E, J, \pi) \rangle$ (not to be confused with the GDR width) is related to the total photon transmission coefficient by $\langle \Gamma_\gamma(E, J, \pi) \rangle = T_\gamma(E, J, \pi) / (2\pi\rho(E, J, \pi))$. This way the nuclear level density (which will be discussed in the next subsection) enters in the average radiation width. Extensive sets of measured average radiation widths come from thermal s-wave ($l = 0$) neutron capture, the relevant theoretical quantity to be compared with such experimental data is

$$\langle \Gamma_\gamma \rangle_0 = \frac{J_i + 1}{2J_i + 1} \langle \Gamma_\gamma(S_n, J_i + 1/2, \pi_i) \rangle + \frac{J_i}{2J_i + 1} \langle \Gamma_\gamma(S_n, J_i - 1/2, \pi_i) \rangle, \quad (32)$$

where S_n is the compound nucleus neutron separation energy and $J_i(\pi_i)$ is the spin (parity) of the target nucleus. Utilizing the methods outlined above within a macroscopic-microscopic approach for the Lorentzian form of the E1 giant dipole resonance leads to a global agreement generally within a factor of 1.5 for nuclei experimentally accessible. This involves a correction to an energy-dependent width due to the fact, that for low energy gamma-transitions which are part of the Giant resonance, the Lorentz curve is suppressed and, in addition, the GDR width increases with excitation energy. This led to $\Gamma_G(E_\gamma) = \Gamma_G \times (E_\gamma/E_G)^\delta$ with $\delta=0.5$ (McCullagh et al, 1981), for a slightly different term (close to $\delta = 1$) have a look at Goriely and Plujko (2019).

An additional entity of the low-lying E1 response below the GDR energy was experimentally noticed (see e.g. Goriely, 1998, termed as Pigmy dipole resonance PDR) and led other authors (Junghans et al, 2008) to an artificial broadening of the GDR with a $\delta=1.5$ (see the broader curve in Fig.10). Microscopically it can be well described by Skyrme+QRPA or RMF+cQRPA approaches, macroscopically it is interpreted as an oscillation of the neutron skin against the $N = Z$ core. Further investigations into this topic have been undertaken theoretically and experimentally (e.g Litvinova et al, 2009; Guttormsen et al, 2022). An approximate description for the E1 PDR within a phenomenological macroscopic approach, based on the neutron skin thickness, has been provided (van Isacker et al, 1992) and utilized (Goriely, 1998). Recent developments include an advanced understanding of the PDR (with E1 and M1 contributions) and its total effect on capture cross sections (Markova et al, 2021; Guttormsen et al, 2022) as shown in Fig.12.

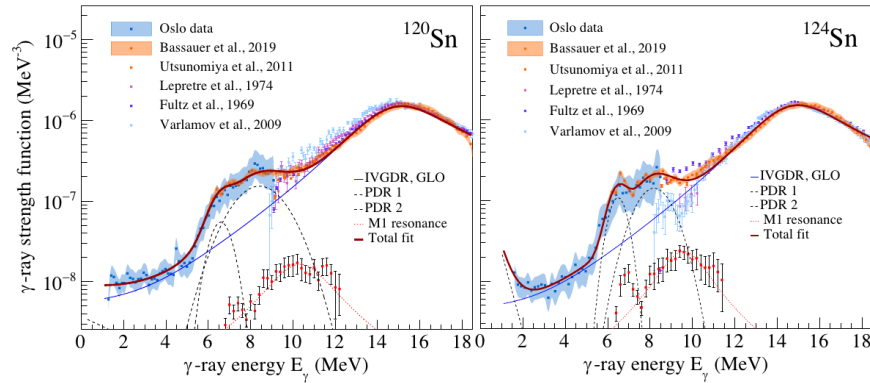


Fig. 12 (courtesy of M. Markova) Total gamma ray strength function as a function of transition energy (see also Fig.10) for two Sn isotopes. See especially the contribution of the low-lying strength in the E1 PDR, the two M1 spin flip and scissor mode contributions, and the upbend at lowest energies.

Various treatments are available for the M1 giant resonance in a similar functional form as discussed above in Eq.(29), but with typically smaller resonance energies and widths and a smaller normalisation factor (see the M1 component in Fig.12). This involves two M1 modes, the spin-flip and the scissor mode (the latter only present in deformed nuclei), for which empirical expressions have been derived in Goriely and Plujko (2019) in forms identical to Eq.(31), but with different scaling factors and typical resonance energies around 7-10 MeV, respective 2.5-4 MeV and corresponding widths of about 4 respective 1.5 MeV (for shell model based predictions see e.g. Loens et al, 2008; Sieja, 2018). An additional effect relates to the fact that for small energies the Brink hypothesis (the transition strength as a function of energy is independent of the excitation energy of the state) is apparently broken at low energies, leading to a different behavior for absorption in comparison to de-excitation. This results, based on shell model calculations, in a constant limit towards lowest energies for the E1 strength and an upbend in case of the M1 strength (Goriely et al, 2018; Goriely and Plujko, 2019). The effects can nicely be seen in Fig.12, with the upbend at lowest energies, the two M1 modes, and an extended E1 PDR. While the low-lying E1 strength contributes only on the less than 10% level close to stability, for very neutron-rich nuclei with an extended neutron skin it can lead to large enhancements and the low-lying M1 strength and especially the upband at lowest energies can have a quite sizable effect close to the neutron drip line.

Another effect has to be taken into account for alpha-capture reactions on self-conjugate ($N = Z$) nuclei, because due to isospin selection rules γ -transitions between isospin $I = 0$ levels are forbidden. This leads to a suppression of corresponding alpha-capture cross sections which can be treated via a suppression of the appropriate γ -transitions (Rauscher et al, 2000).

Fission

Along the valley of stability, actinide and transuranic nuclei become increasingly unstable as a result of fission in their ground states. This loss of stability arises because the disruptive Coulomb force, which increases as Z^2 , overcomes the cohesive surface tension, proportional to $A^{2/3}$. The nuclear mass, i.e. potential energy for a given (Z, A) , as a function of deformation, has a local minimum at the ground state deformation. It first increases with increasing deformation until reaching a maximum at the saddle point, from which point onward fission is inevitable. This potential barrier (=fission barrier) can have very small tunneling transmission coefficients and therefore very long fission half-lives. While the simple liquid-drop approach to nuclear masses leads only to a single barrier plotted as a function of deformation, the barrier is in most cases split into a double-humped (or even multiple) barrier prescription, due to shell effects (Strutinsky, 1967, 1968). The higher of the peaks is denoted the fission barrier, since states beyond that excitation energy can actually fission instantaneously.

More generally, the mass (potential energy) can be evaluated not only along a deformation path but rather as a function of several deformation parameters. One possibility is the choice of utilizing the parameters elongation, neck diameter, left-fragment spheroidal deformation, right-fragment spheroidal deformation, and nascent-fragment mass asymmetry. Fig. 13 (top panel) shows such a potential energy contour plot for ^{232}Th (Möller et al, 2015). Because the potential energy (=mass) as a function of deformation must be calculated for a particular choice of mass model, many theoretical efforts have been undertaken (see e.g. Schunck and Regnier, 2022, and references therein) and the results will be dependent on these mass models. Fig. 14 gives the results of Möller et al (2015). Investigations utilized in astrophysical applications developed from 1980 until present (see e.g. Howard and Möller, 1980; Myers and Świątecki, 1999; Mamdouh et al, 2001; Goriely et al, 2009; Vassh et al, 2019; Giuliani et al, 2020).

For most of the actinides the fission barrier development as a function of deformation can be described within the so-called double-humped fission barrier (Bjørnholm and Lynn, 1980) and the fission probability can be calculated within the complete-damping formalism, making use of two Hill-Wheeler inverted parabola barriers (Lynn and Back, 1974), as utilized in a number of applications (Thielemann et al, 1983; Panov et al, 2005, 2010) (see Fig. 13, bottom panel), otherwise a more complex quantum mechanical approach for the penetration through the barrier potential has to be performed (Goriely et al, 2009).

As discussed previously, excited states close to or above the fission barrier will have much shorter fission half-lives than ground states, and therefore processes like neutron capture or beta-decay, which populate excited states of the compound nucleus or daughter nucleus, will lead to increased probabilities for fission relative to the ground state. Therefore, neutron-induced and beta-delayed fission can play an important role in astrophysics, including the the r-process.

The statistical model calculations discussed in this section can be extended to include a fission channel, in order to calculate cross sections for neutron-induced

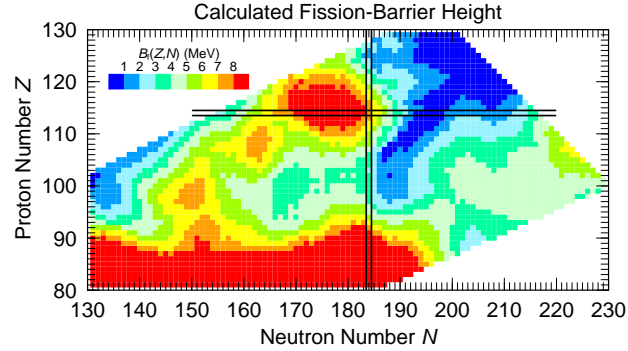


Fig. 14 Fission barrier heights B_f based on macroscopic-microscopic fission potential-energy calculations (Möller et al, 2015). Image provided from the database of P. Möller, see <https://t2.lanl.gov/nis/molleretal/>.

fission probability $P_f(E, J, \pi) = T_f(E, J, \pi)/T_{tot}(E, J, \pi)$. With a value obtained for P_f and the calculated transmission coefficients T_o ($o \neq f$) for all other channels, one can solve $P_f = T_f/(T_f + \sum_{o \neq f} T_o)$ for T_f to be used e.g. for neutron induced cross section predictions (or also beta-delayed fission). For applications to astrophysical question see e.g. (Martinez-Pinedo et al, 2007; Petermann et al, 2012; Erler et al, 2012; Eichler et al, 2015; Giuliani et al, 2018; Eichler et al, 2019; Giuliani et al, 2020; Kullmann et al, 2023; Holmbeck et al, 2023).

Level Densities

The present status of the theoretical understanding of nuclear level densities (one of the most important statistical nuclear properties), from empirical models to microscopic methods, has been given in an excellent review (Alhassid, 2021). Many statistical model calculations use the level density description of the back-shifted Fermi gas (Gilbert and Cameron, 1965)

$$\begin{aligned}
\rho(U, J, \pi) &= 1/2 f(U, J) \rho(U) \\
\rho(U) &= \frac{1}{\sqrt{2\pi}\sigma} \frac{\sqrt{\pi}}{12a^{1/4}} \frac{\exp(2\sqrt{aU})}{U^{5/4}} \\
f(U, J) &= \frac{2J+1}{2\sigma^2} \exp(-J(J+1)/2\sigma^2) \\
\sigma^2 &= \frac{\Theta_{rigid}}{\hbar^2} \sqrt{\frac{U}{a}} \quad \Theta_{rigid} = \frac{2}{5} m_u A R^2 \quad U = E - \delta,
\end{aligned} \tag{33}$$

which assumes that positive and negative parities are evenly distributed and that the spin dependence $f(U, J)$ is determined by the spin cut-off parameter σ . The level density of a nucleus is therefore dependent only on two parameters: the level density parameter a and the backshift δ , which determines the energy of the first excited state. This backshift is related to the level spacing between the last occupied and the first unoccupied state in the single particle shell model and to the pairing gap, the energy necessary to break up a proton or neutron pair. Of these two effects, the pairing energy dominates except in the very near vicinity of closed shells. Within this framework, the quality of level density predictions depends on the reliability of systematic estimates of the level density parameter a and the backshift δ . Eq.(33) provides a valid functional form for reproducing level densities down to an excitation energy of $U = 1-2$ MeV, but it diverges for $U = 0$, i.e. $E = \delta$. This causes problems if δ is a positive backshift. Ericson plots, which show the number of excited states as a function of excitation energy, reveal an almost linear behavior for $\ln(N) = f(E)$ with an intercept at $E = E_0 = \delta$ (Ericson, 1959). This resulted in the ansatz $\rho(U) = \exp(U/T)/T$, commonly called the constant temperature formula. The two formulations can be combined for low and high excitation energies, with $E_0 = \delta$ and T being determined by a tangential fit to the Fermi gas formula. This description is usually called the composite (Gilbert-Cameron) formula.

The first compilation of a and δ was provided for a large number of nuclei by Gilbert and Cameron (1965). They found that the backshift δ is well reproduced by experimental pairing corrections. Theoretical predictions result in $a/A \approx 1/15$ for infinite nuclear matter, but the inclusion of surface and curvature effects of finite nuclei enhances this value to $1/6 - 1/8$. While in principle a can be dependent on temperature or excitation energy, such a dependence is minimal for excitation energies up to $3 \times A$ (MeV) and thus the zero temperature value for a can be used up to these energies, covering all values of interest within the present context. When comparing experimentally derived values of a with such a simple formulation, one notices large deviations due to shell effects (nuclei near closed shells have much smaller values for a). An empirical correlation with experimental shell corrections $S(N, Z)$ was realized (Gilbert and Cameron, 1965)

$$a/A = c_0 + c_1 S(N, Z), \tag{34}$$

where $S(N, Z)$ is negative near closed shells. Many other functional dependencies have been proposed and more microscopic treatments have been carried out (see e.g.

[Goriely et al, 2012](#)). If one constructs level densities from single particle spectra, it means that large care has to be invested in predicting correct single particle spectra.

There have been a number of compilations for a and δ , or T and E_0 , based on purely experimental level densities, but predictions for unstable nuclei or those for which experimental information is not available have to be based on theory, including the predictions for shell and pairing corrections. For a review of early investigations see [Cowan et al \(1991\)](#), utilizing the pairing corrections of a droplet nuclear mass model. Such an average behavior changes, however, within one unit of magic nucleon numbers, where the backshifts are often much larger.

Deformed nuclei should in principle, be treated differently, as a rotational band can be associated with each excited state. At high excitation energies this treatment can, however, lead to double counting. Another option is to keep the same formalism as in Eq.(34) but performing an independent evaluation of the coefficients c_0 and c_1 for deformed nuclei, because only one parameter set for c_0 and c_1 , cannot achieve a significantly better agreement with experimental level densities than found in [Gilbert and Cameron \(1965\)](#) with a deviations up to a factor of 10. By dividing the nuclei into three classes (a: those within three units of magic nucleon numbers, b: other spherical nuclei, c: deformed nuclei), an improved agreement was obtained (maximum deviations of less than a factor of 3 where experimental information at the neutron separation energy is available) ([Cowan et al, 1991](#)). However, this treatment was still very phenomenological and led [Rauscher et al \(1997\)](#) to make use of an improved approach, considering that the energy dependence of the shell effects vanish at high excitation energies. Although, for astrophysical purposes only energies close to the particle separation thresholds have to be considered, an energy dependence can lead to a considerable improvement of the global fit. This is especially true for strongly bound nuclei close to magic numbers. An excitation-energy dependent description has been proposed for the level density parameter a ([Ignatyuk et al, 1980](#))

$$\begin{aligned}
 a(U, Z, N) &= \tilde{a}(A) \left[1 + C(Z, N) \frac{f(U)}{U} \right] \\
 \tilde{a} &= \alpha A + \beta A^{2/3} \\
 f(U) &= 1 - \exp(-\gamma U).
 \end{aligned}
 \tag{35}$$

The values of the free parameters a , b , and γ can be determined by fitting to experimental level density data. The shape of the function $f(U)$ permits the two extremes (i) for small excitation energies the original form of Eq.(34) is retained with $S(Z, N)$ being replaced by $C(Z, N)$ and (ii) for high excitation energies a/A approaches the continuum value obtained for infinite nuclear matter (for details see [Rauscher et al, 1997](#)).

The approach to the backshift δ could be improved further by utilizing the masses of neighboring nuclei (from experiment or mass models if those are not available) in order to obtain a more realistic pairing correction. When obtaining the pairing correction directly from the masses with

$$\begin{aligned}
\delta &= \frac{1}{2}[\Delta_n + \Delta_p] \\
\Delta_n &= \frac{1}{2}[-M(A-1, Z) + 2M(A, Z) - M(A+1, Z)] \\
\Delta_p &= \frac{1}{2}[-M(A-1, Z-1) + 2M(A, Z) - M(A+1, Z+1)]
\end{aligned} \tag{36}$$

better fits to the total level density could be achieved with experimental level densities at the neutron separation energy within a factor of 2 to 3, as utilized in the NON-SMOKER code. Parity-dependent level density descriptions (not using the factor 1/2 in Eq.(33) have also been utilized for tests in application to cross section predictions (Mocelj et al, 2007; Loens et al, 2008) and are the default option in the code SMARAGD.

Width Fluctuation Corrections

In addition to the ingredients required for Eq.(25), like the transmission coefficients for particles and photons and the level densities, width fluctuation corrections $W(j, o, J, \pi)$ have to be employed. They define the correlation factors with which all partial channels of incoming particle j and outgoing particle o , passing through excited state (E, J, π) , have to be multiplied. This is due to the fact that the decay of the state is not fully statistical, but some memory of the way of formation is retained and influences the available decay choices. The major effect is elastic scattering, the incoming particle can be immediately re-emitted before the nucleus equilibrates. Once the particle is absorbed and not re-emitted in the very first (pre-compound) step, the equilibration is very likely. This corresponds to enhancing the elastic channel by a factor W_j . The NON-SMOKER code uses the description of Tepel et al (1974), leading to Eqs.(37) and (38). In order to conserve the total cross section, the individual transmission coefficients in the outgoing channels have to be renormalized to T'_j . The total cross section is proportional to T_j and one obtains the condition $T_j = T'_j(W_j T'_j / T'_{tot}) + T'_j(T'_{tot} - T'_j) / T'_{tot}$. This can be (almost) solved for T'_j

$$T'_j = \frac{T_j}{1 + T'_j(W_j - 1) / T'_{tot}}. \tag{37}$$

This approach requires an iterative solution for T' (starting in the first iteration with T_j and T'_{tot}), which converges fast. The enhancement factor W_j have to be known in order to apply Eq.(37), a general expression in closed form is very complicated and computationally expensive to employ. A fit to results from Monte Carlo calculations (Tepel et al, 1974) leads to

$$W_j = 1 + \frac{2}{1 + T_j^{1/2}}. \tag{38}$$

For a general discussion of approximation methods (see e.g. [Gadioli and Hodgson, 1992](#)). There exist further expressions for this renormalization ([Hofmann et al, 1980](#); [Moldauer, 1980](#)) which are utilized as options in the TALYS code. The NON-SMOKER code makes use of [Tepel et al \(1974\)](#) with Eqs.(37) and (38), which redefine the transmission coefficients in Eq.(26) in such a manner that the total width is redistributed by enhancing the elastic channel and weak channels over the dominant one. While this is only an approximation to the correct treatment, it could be shown that this treatment is quite adequate [Thomas et al \(1986\)](#).

Cross section applications

Our discussion in the previous subsections reveals that one can expect to obtain good agreement with experiment for particle and photon transmission coefficients in comparison to experiments. On the other hand, level density predictions which are based on shell correction terms of microscopic-macroscopic mass models, show a statistical spread (a factor of 2 at the neutron separation energy). But all this applies to nuclei where experimental information is available, and can clearly be larger for nuclei far from stability. Neutron capture cross sections at 30 keV (utilized for many astrophysical applications) of the NON-SMOKER code show agreement by less than a factor of 2, with a few exceptions for nuclei located specifically at magic numbers. This is a consequence of the still imperfect predictions of nuclear level densities.

This includes the question whether the statistical Hauser-Feshbach formalism can be applied to all nuclei, also far from stability. The statistical model assumes that one can utilize a transmission behavior averaged over resonances. This requires that in the Gamow window for charged particle reactions or in the energy window of a thermal neutron distribution a sufficient number of resonances is available in the compound nucleus. This energy window depends on the temperature in the plasma of reacting nuclei, because in astrophysical applications the reaction rate $\langle\sigma v\rangle$ depends on an integration of the cross section over a thermal distribution of reactants as shown in Eq.(5). Requiring about 10 levels in this thermal window leads to the following applicability criterion for neutron capture cross sections shown in Fig.15. A major question is whether one would need to utilize direct capture predictions for the marginal regions in the nuclear chart, which include large uncertainties ([Mathews et al, 1983](#); [Rauscher et al, 1998](#); [Goriely, 1998](#)), or a modification of the statistical model ([Rauscher, 2011](#)).

Fig.16 shows a comparison of Maxwellian averaged neutron capture cross sections for two Sn isotopes as a function of environment temperature. One can see that (still close to stability) the predictions of NON-SMOKER and the various options in the TALYS code provide a quite reasonable prediction within a factor of 2. The enhanced gamma-strength function due to low-lying strength of the PDR, M1 contributions and an upbend at lowest energies (see the subsection on γ -transmission coefficients), which can be included in the TALYS code, could, however, increase the difference between both codes for neutron-rich nuclei far from stability.

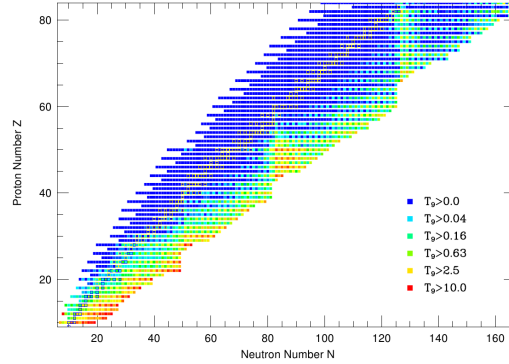


Fig. 15 Required minimum temperatures for the applicability of the Hauser-Feshbach statistical model for neutron capture reactions, based on the request that about 10 resonances (levels) exist in the thermal energy window when utilizing a specific level density description (Rauscher et al, 1997). While in most explosive nucleosynthesis application such conditions are fulfilled, r-process applications in the range of $1\text{-}3 \times 10^9 \text{K}$ might be marginal close to the neutron-drip line just above neutron shell closures. These predictions were done by utilizing the microscopic-macroscopic FRDM model (Möller et al, 1995), updates of this mass model and microscopic level density treatments might improve this situation. A similar plot for alpha-capture reactions (Rauscher et al, 1997) leads to the conclusion that no temperature restrictions apply, because alpha-capture Q-values do not experience such a dependence of the distance from stability. For proton-capture reactions restrictions also apply close to the proton-drip line up to $Z \approx 30$, requiring temperatures in excess of $2.5 \times 10^9 \text{K}$ (Rauscher, 2011, 2020). Image reproduced with permission of Rauscher et al (1997), copyright by APS.

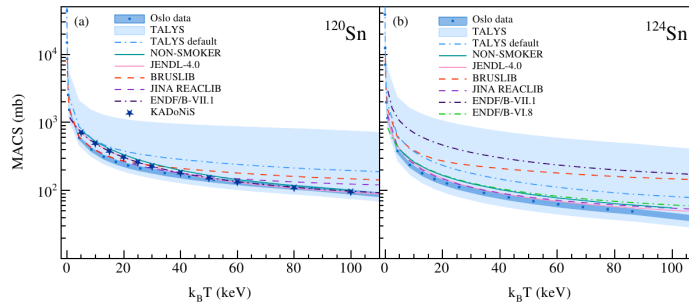


Fig. 16 (Courtesy of M. Markova) Maxwellian averaged neutron capture cross section prediction for the Sn isotopes 120 and 124 as a function of the astrophysical environment temperature. Shown are the results based on experiments and the predictions of the NON-SMOKER as well as TALYS codes (for the latter indicates the spread, which results from the variety of options available).

At this point we also show some energy-dependent cross section evaluations for charged particle reactions involving intermediate mass nuclei which play an important role in silicon burning. Fig. 17 indicates the importance of width fluctuation corrections when at a specific energy another reaction channel opens.

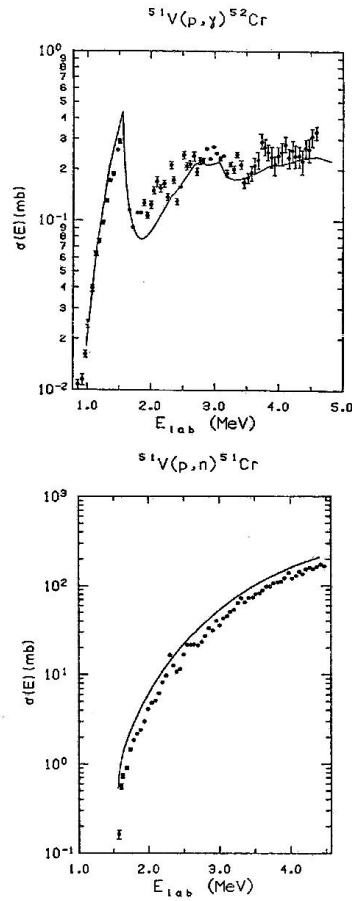


Fig. 17 Cross section prediction for the reactions $^{51}\text{V}(p, \gamma)$ and $^{51}\text{V}(p, n)$, utilizing width fluctuation corrections (Tepel et al, 1974). Without this correction the capture cross section would be enhanced by a factor of 4 beyond the neutron channel opening at 1.6 MeV. Image reproduced with permission from Cowan et al (1991), copyright by Elsevier.

Finally we want to present also some results of fission cross section predictions (Panov et al, 2010), which show that the procedure to predict these cross sections works quite well, but is highly sensitive to the quality of fission barrier predictions, when applied for unstable nuclei without experimental determinations of the fission barriers. Fig. 18 shows the prediction of neutron induced fission cross sections as a function of energy, (a) in comparison to experiments and (b) when applying different theoretical fission barrier predictions, Fig. 19 shows the astrophysical reaction rates as a function of environment temperature, also indicating when neutron energies surpass the fission barrier energies.

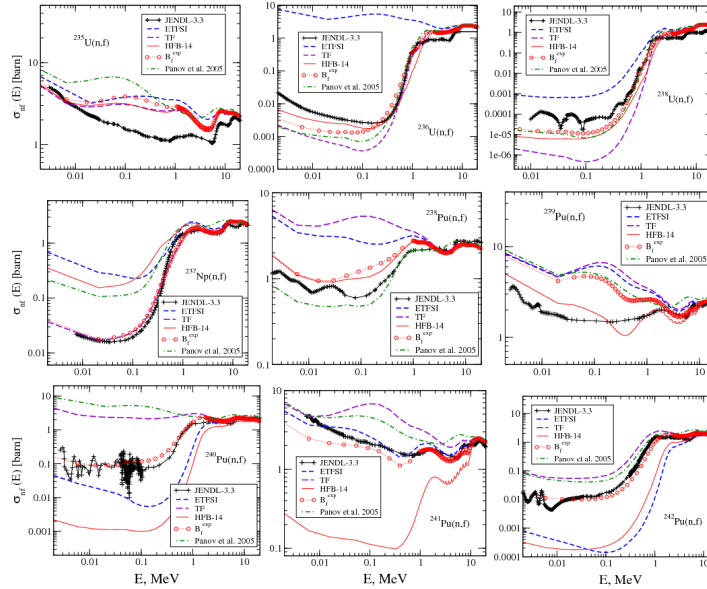


Fig. 18 Neutron-induced fission cross sections predictions for a variety of actinide nuclei (Panov et al, 2010, 2005) in comparison to experiments from JENDL-3.3 (crosses Nakagawa et al, 2005), averaged by the code JANIS (black lines Soppera et al, 2011). It is clearly seen that the quality of theoretical fission barrier predictions (ETFSI, TF, HFB-14, Mamdouh et al, 2001; Myers and Świątecki, 1999; Goriely et al, 2009) affects the results strongly. Image reproduced with permission from Panov et al (2010), copyright by ESO.

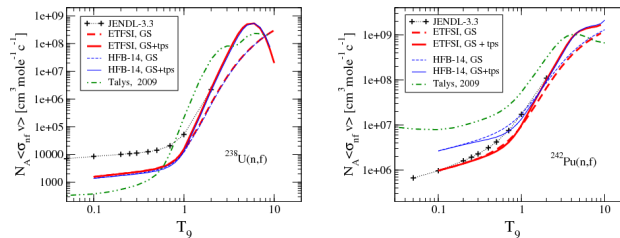


Fig. 19 Similar to Fig. 18, but for astrophysical neutron-induced fission reaction rates as a function of environment temperature (Panov et al, 2010), utilizing either only the target ground state or thermally populated targets, which have an effect on the opening of the fission channel. TALYS (2009) stands for Goriely et al (2009), who include a thermal target population. Image reproduced with permission from Panov et al (2010), copyright by ESO.

Summary

In the present Handbook chapter we examined the nuclear reactions in evolving stars, starting with hydrostatic burning phases of stellar evolution and continuing through explosive burning in various astrophysical environments, taking place in supernovae or explosive binary events. Important reactions were listed in Tables 1 through

7, going over to features being accompanied with the transition from dominating individual reactions to nuclear statistical equilibrium NSE in Figs. 1 through 4. Finally regions of the nuclear chart were identified, where nuclear reaction input is required for the different explosive nucleosynthesis processes. While the early phases of stellar burning, involving mostly light to intermediate mass nuclei, need to be tackled mostly by experimental approaches (see the chapter by M. Wiescher, J. deBoer & R. Reifarth), for intermediate and heavy nuclei - with a high density of levels at the bombarding energy - statistical model (Hauser-Feshbach) approaches can be applied. This topic has been followed in detail, including the treatment of particle channels, gamma-transitions, fission, and level density predictions, also for nuclei far from stability.

While our focus has been on charged-particle and neutron-induced reactions, we only mentioned the influence and importance of weak interactions in stellar environments, e.g. in late burning stages and in stellar explosions, but want to refer here to the chapters by Suzuki (and [Langanke et al, 2021](#)) on electron capture reactions, and Rrapaj & Reddy, Fuller & Grohs, Wang & Surman, Famiano et al., Fröhlich, Wanajo, and Obergaulinger on the role of neutrino reactions in evolving stars and their explosive endpoint.

Finally it should be mentioned, that the recent white paper on nuclear astrophysics ([Schatz et al, 2022](#)) is an enormous resource for presently ongoing experimental efforts from cross section measurements at astrophysical energies to investigations of nuclear properties with radioactive ion beam facilities far from stability. Experiments at underground facilities with the aim to measure at lowest possible energies, avoiding background noise are ongoing, e.g., at LUNA⁵, CASPAR⁶ and JUNA ([Liu et al, 2022](#)).

On the theoretical side extended compilations for reaction rate predictions are provided in several publicly available database^{7, 8, 9, 10}, including results from the previously described codes NON-SMOKER and TALYS. All of these resources provide the input for the understanding of nuclear transmutations by reactions in evolving stars and their catastrophic endpoints (for a more general overview about the astrophysical sites contributing to the cosmic abundances of all chemical elements and their role in the evolution of galaxies see, e.g., [Arcones and Thielemann, 2023](#)).

⁵ <https://luna.lngs.infn.it/index.php/new-about-us>

⁶ <https://caspar.nd.edu/>

⁷ <https://www.jinaweb.org/science-research/scientific-resources>

⁸ <https://nuastro.org>

⁹ <https://reaclib.jinaweb.org>

¹⁰ <https://www-nds.iaea.org>

Acknowledgements

This article benefited from exchange and interactions within the European COST Action CA16117 Chemical Elements as Tracers of the Evolution of the Cosmos (ChETEC), and the International Research Network for Nuclear Astrophysics (IRENA). We also want to thank a large number of colleagues for communication and exchange related to the present overview, to name a few: Michael Wiescher, Ken'ichi Nomoto, Gabriel Martinez-Pinedo, Elena Litvinova, Maria Markova, Igor Panov, and Stephane Goriely.

References

- Adelberger EG, Garcia A, Robertson RGH, Snover KA, Balantekin AB, Heeger K, Ramsey-Musolf MJ, Bemmerer D, Junghans A, Bertulani CA, Chen JW, Costantini H, Prati P, Couder M, Uberseder E, Wiescher M, Cyburt R, Davids B, Freedman SJ, Gai M, Gazit D, Gialanella L, Imbriani G, Greife U, Hass M, Haxton WC, Itahashi T, Kubodera K, Langanke K, Leitner D, Leitner M, Vetter P, Winslow L, Marcucci LE, Motobayashi T, Mukhamedzhanov A, Tribble RE, Nollett KM, Nunes FM, Park TS, Parker PD, Schiavilla R, Simpson EC, Spitaleri C, Strieder F, Trautvetter HP, Suemmerer K, Typel S (2011) Solar fusion cross sections. II. The pp chain and CNO cycles. *Rev Mod Phys* 83(1):195–246, DOI 10.1103/RevModPhys.83.195, [1004.2318](#)
- Alhassid Y (2021) Nuclear level densities: From empirical models to microscopic methods. In: Escher J, Alhassid Y, Bernstein LA, Brown D, Fröhlich C, Talou P, Younes W (eds) *Compound-Nuclear Reactions*, Springer International Publishing, Cham, pp 97–112
- Amarsi AM, Grevesse N, Asplund M, Collet R (2021) The solar carbon, nitrogen, and oxygen abundances from a 3D LTE analysis of molecular lines. *Astron & Astrophys* 656:A113, DOI 10.1051/0004-6361/202141384, [2109.04752](#)
- Anders E, Grevesse N (1989) Abundances of the elements: Meteoritic and solar. *Geochem Cosmochem Acta* 53(1):197–214, DOI 10.1016/0016-7037(89)90286-X
- Angulo C, Arnould M, Rayet M, Descouvemont P, Baye D, Leclercq-Willain C, Coc A, Barhoumi S, Aguer P, Rolfs C, Kunz R, Hammer JW, Mayer A, Paradellis T, Kossionides S, Chronidou C, Spyrou K, degl'Innocenti S, Fiorentini G, Ricci B, Zavatarelli S, Providencia C, Wolters H, Soares J, Grama C, Rahighi J, Shotton A, Laméhi Rachti M (1999) A compilation of charged-particle induced thermonuclear reaction rates. *Nucl Phys A* 656(1):3–183, DOI 10.1016/S0375-9474(99)00030-5
- Arcones A, Thielemann FK (2023) Origin of the elements. *Astron & Astrophys Rev* 31(1):1, DOI 10.1007/s00159-022-00146-x
- Arnould M (1972) Influence of the Excited States of Target Nuclei in the Vicinity of the Iron Peak on Stellar Reaction Rates. *Astron & Astrophys* 19:92
- Asplund M, Grevesse N, Sauval AJ, Scott P (2009) The Chemical Composition of the Sun. *Annu Rev Astron Astrophys* 47:481–522, DOI 10.1146/annurev.astro.46.060407.145222
- Bahcall N John (1989) *Neutrino Astrophysics*. Cambridge University Press, Cambridge
- Berman BL, Fultz SC (1975) Measurements of the giant dipole resonance with monoenergetic photons. *Rev Mod Phys* 47(3):713–761, DOI 10.1103/RevModPhys.47.713
- Bjørnholm S, Lynn JE (1980) The double-humped fission barrier. *Rev Mod Phys* 52(4):725–931, DOI 10.1103/RevModPhys.52.725
- Bruno CG, Scott DA, Aliotta M, Formicola A, Best A, Boeltzig A, Bemmerer D, Broggini C, Cacioli A, Cavanna F, Ciani GF, Corvisiero P, Davinson T, Depalo R, Di Leva A, Elekes Z, Ferraro F, Fülöp Z, Gervino G, Guglielmetti A, Gustavino C, Gyürky G, Imbriani G, Junker M, Menegazzo R, Mossa V, Pantaleo FR, Piatti D, Prati P, Somorjai E, Straniero O, Strieder

- F, Szücs T, Takács MP, Trezzi D, LUNA Collaboration (2016) Improved Direct Measurement of the 64.5 keV Resonance Strength in the $^{17}\text{O} (p, \alpha)^{14}\text{N}$ Reaction at LUNA. *Phys Rev Lett* 117(14):142502, DOI 10.1103/PhysRevLett.117.142502, [1610.00483](https://doi.org/10.1103/PhysRevLett.117.142502)
- Caughlan GR, Fowler WA (1988) Thermonuclear Reaction Rates V. *At Data Nucl Data Tables* 40:283, DOI 10.1016/0092-640X(88)90009-5
- Cescutti G, Molaro P (2019) ^7Li evolution in the thin and thick discs of the Milky Way. *Mon Not Roy Astron Soc* 482(4):4372–4382, DOI 10.1093/mnras/sty2967, [1810.12215](https://doi.org/10.1093/mnras/sty2967)
- Cowan JJ, Thielemann FK, Truran JW (1991) The r-process and nucleochronology. *Phys Rep* 208:267–394, DOI 10.1016/0370-1573(91)90070-3
- Cowan JJ, Sneden C, Lawler JE, Aprahamian A, Wiescher M, Langanke K, Martinez-Pinedo G, Thielemann FK (2021) Origin of the heaviest elements: The rapid neutron-capture process. *Rev Mod Phys* 93(1):015002, DOI 10.1103/RevModPhys.93.015002, [1901.01410](https://doi.org/10.1103/RevModPhys.93.015002)
- Curtis S, Ebinger K, Fröhlich C, Hempel M, Perego A, Liebendörfer M, Thielemann FK (2019) PUSHing Core-collapse Supernovae to Explosions in Spherical Symmetry. III. Nucleosynthesis Yields. *Astrophys J* 870:2, DOI 10.3847/1538-4357/aae7d2
- Cyburtt RH, Amthor AM, Ferguson R, Meisel Z, Smith K, Warren S, Heger A, Hoffman RD, Rauscher T, Sakharuk A, Schatz H, Thielemann FK, Wiescher M (2010) THE JINA REACLIB DATABASE: ITS RECENT UPDATES AND IMPACT ON TYPE-I X-RAY BURSTS. *Astrophys J Suppl* 189(1):240–252, DOI 10.1088/0067-0049/189/1/240, URL <https://doi.org/10.1088/0067-0049/189/1/240>
- Danos M (1958) On the long-range correlation model of the photonuclear effect. *Nuclear Physics* 5:23–32, DOI 10.1016/0029-5582(58)90005-1
- deBoer RJ, Görres J, Wiescher M, Azuma RE, Best A, Brune CR, Fields CE, Jones S, Pignatari M, Sayre D, Smith K, Timmes FX, Uberseder E (2017) The $^{12}\text{C}(\alpha, \gamma)^{16}\text{O}$ reaction and its implications for stellar helium burning. *Rev Mod Phys* 89(3):035007, DOI 10.1103/RevModPhys.89.035007, [1709.03144](https://doi.org/10.1103/RevModPhys.89.035007)
- Eichler M, Arcones A, Kelic A, Korobkin O, Langanke K, Marketin T, Martinez-Pinedo G, Panov I, Rauscher T, Rosswog S, Winteler C, Zinner NT, Thielemann FK (2015) The role of fission in neutron star mergers and its impact on the r-process peaks. *Astrophys J* 808:30, DOI 10.1088/0004-637X/808/1/30
- Eichler M, Sayar W, Arcones A, Rauscher T (2019) Probing the Production of Actinides under Different r-process Conditions. *Astrophys J* 879:47, DOI 10.3847/1538-4357/ab24cf
- Ericson T (1959) A statistical analysis of excited nuclear states. *Nuclear Physics* 11:481–491, DOI 10.1016/0029-5582(59)90291-3
- Erler J, Langanke K, Loens H, Martinez-Pinedo G, Reinhard PG (2012) Fission properties for r-process nuclei. *Phys Rev C* 85:025802, DOI 10.1103/PhysRevC.85.025802
- Febbraro M, deBoer RJ, Pain SD, Toomey R, Becchetti FD, Boeltzig A, Chen Y, Chipps KA, Couder M, Jones KL, Lamere E, Liu Q, Lyons S, Macon KT, Morales L, Peters WA, Robertson D, Rasco BC, Smith K, Seymour C, Seymour G, Smith MS, Stech E, Kolk BV, Wiescher M (2020) New $^{13}\text{C}(\alpha, n)^{16}\text{O}$ Cross Section with Implications for Neutrino Mixing and Geoneutrino Measurements. *Phys Rev Lett* 125(6):062501, DOI 10.1103/PhysRevLett.125.062501
- Formicola A, Corvisiero P, Gervino G (2016) The nuclear physics of the hydrogen burning in the Sun. *Eur Phys J A* 52(4):73, DOI 10.1140/epja/i2016-16073-6
- Fowler WA, Caughlan GR, Zimmerman BA (1967) Thermonuclear Reaction Rates. *Annu Rev Astron Astrophys* 5:525, DOI 10.1146/annurev.aa.05.090167.002521
- Fröhlich C, Martinez-Pinedo G, Liebendörfer M, Thielemann FK, Bravo E, Hix WR, Langanke K, Zinner NT (2006) Neutrino-induced nucleosynthesis of $A > 64$ nuclei: The νp -process. *Phys Rev Lett* 96:142502, DOI 10.1103/PhysRevLett.96.142502
- Gadioli E, Hodgson PE (1992) *Pre-Equilibrium Nuclear Reactions*. Clarendon Press Oxford
- Ghosh S, Wolfe N, Fröhlich C (2022) PUSHing Core-collapse Supernovae to Explosions in Spherical Symmetry. V. Equation of State Dependency of Explosion Properties, Nucleosynthesis Yields, and Compact Remnants. *Astrophys J* 929(1):43, DOI 10.3847/1538-4357/ac4d20, [2107.13016](https://doi.org/10.3847/1538-4357/ac4d20)

- Gilbert A, Cameron AGW (1965) A composite nuclear-level density formula with shell corrections. *Canadian Journal of Physics* 43:1446, DOI 10.1139/p65-139
- Giuliani SA, Martinez-Pinedo G, Robledo LM (2018) Fission properties of superheavy nuclei for r -process calculations. *Phys Rev C* 97(3):034323, DOI 10.1103/PhysRevC.97.034323, [1704.00554](#)
- Giuliani SA, Martinez-Pinedo G, Wu MR, Robledo LM (2020) Fission and the r -process nucleosynthesis of translead nuclei in neutron star mergers. *Phys Rev C* 102(4):045804, DOI 10.1103/PhysRevC.102.045804, [1904.03733](#)
- Goriely S (1998) Radiative neutron captures by neutron-rich nuclei and the r -process nucleosynthesis. *Phys Lett B* 436:10–18
- Goriely S, Plujko V (2019) Simple empirical $E1$ and $M1$ strength functions for practical applications. *Phys Rev C* 99(1):014303, DOI 10.1103/PhysRevC.99.014303
- Goriely S, Hilaire S, Koning AJ (2008) Improved microscopic nuclear level densities within the Hartree-Fock-Bogoliubov plus combinatorial method. *Phys Rev C* 78:064307, DOI 10.1103/PhysRevC.78.064307
- Goriely S, Hilaire S, Koning AJ, Sin M, Capote R (2009) Towards a prediction of fission cross sections on the basis of microscopic nuclear inputs. *Phys Rev C* 79:024612, DOI 10.1103/PhysRevC.79.024612
- Goriely S, Hilaire S, Girod M (2012) Latest development of the combinatorial model of nuclear level densities. In: *Journal of Physics Conference Series*, vol 337, p 012027, DOI 10.1088/1742-6596/337/1/012027
- Goriely S, Hilaire S, Péru S, Sieja K (2018) Gogny-hfb+qrpa dipole strength function and its application to radiative nucleon capture cross section. *Phys Rev C* 98:014327, DOI 10.1103/PhysRevC.98.014327, URL <https://link.aps.org/doi/10.1103/PhysRevC.98.014327>
- Görres J, Wiescher M, Thielemann FK (1995) Bridging the waiting points: The role of two-proton capture reactions in the r process. *Phys Rev C* 51:392
- Guttormsen M, Ay KO, Ozgur M, Algin E, Larsen AC, Bello Garrote FL, Berg HC, Crespo Campo L, Dahl-Jacobsen T, Furmyr FW, Gjestvang D, Görger A, Hagen TW, Ingeberg VW, Kheswa BV, Kullmann IKB, Klinte fjord M, Markova M, Midtbø JE, Modamio V, Paulsen W, Pedersen LG, Renstrøm T, Sahin E, Siem S, Tveten GM, Wiedeking M (2022) Evolution of the γ -ray strength function in neodymium isotopes. *Phys Rev C* 106(3):034314, DOI 10.1103/PhysRevC.106.034314
- Heine M, Fruet G, Courtin S, Jenkins DG, Adsley P, Brown A, Canavan R, Catford WN, Charon E, Curien D, Della Negra S, Duprat J, Hammache F, Lesrel J, Lotay G, Meyer A, Monprivat E, Montanari D, Morris L, Moukaddam M, Nippert J, Podolyák Z, Regan PH, Ribaud I, Richer M, Rudigier M, Shearman R, de Séréville N, Stodel C (2022) Direct Measurement of Carbon Fusion at Astrophysical Energies with Gamma-Particle Coincidences. In: *European Physical Journal Web of Conferences*, European Physical Journal Web of Conferences, vol 260, p 01004, DOI 10.1051/epjconf/202226001004
- Hix WR, Thielemann FK (1996) Silicon Burning. I. Neutronization and the Physics of Quasi-Equilibrium. *Astrophys J* 460:869, DOI 10.1086/177016, [astro-ph/9511088](#)
- Hix WR, Thielemann FK (1999) Computational methods for nucleosynthesis and nuclear energy generation. *J Comput Appl Math* 109:321–351, DOI 10.1016/S0377-0427(99)00163-6
- Hofmann HM, Mertelmeier T, Herman M, Tepel JW (1980) Hauser-Feshbach calculations in the presence of weakly absorbing channels with special reference to the elastic enhancement factor and the factorization assumption. *Zeitschrift für Physik A Hadrons and Nuclei* 297(2):153–160, DOI 10.1007/BF01421472
- Holmbeck EM, Sprouse TM, Mumpower MR (2023) Nucleosynthesis and observation of the heaviest elements. *European Physical Journal A* 59(2):28, DOI 10.1140/epja/s10050-023-00927-7, [2304.01850](#)
- Holmes JA, Woosley SE, Fowler WA, Zimmerman BA (1976) Tables of Thermonuclear-Reaction-Rate Data for Neutron-Induced Reactions on Heavy Nuclei. *At Data Nucl Data Tables* 18:305, DOI 10.1016/0092-640X(76)90011-5

- Howard WM, Möller P (1980) Calculated Fission Barriers, Ground-State Masses, and Particle Separation Energies for Nuclei with $76 \leq Z \leq 100$ and $140 \leq N \leq 184$. *At Data Nucl Data Tables* 25:219, DOI 10.1016/0092-640X(80)90005-4
- Ignatyuk AV, Istekov KK, Okolovich VN, Smirenkin GN (1980) Level density and fission probability in spherical and deformed nuclei. In: Presented at the IAEA Symp. on Phys. and Chem. of Fission, pp 14–18
- Ishkhanov BS, Kapitonov IM (2021) Giant dipole resonance of atomic nuclei. prediction, discovery, and research. *Physics-Uspekhi* 64(2):141–156, DOI 10.3367/ufne.2020.02.038725, URL <https://doi.org/10.3367/ufne.2020.02.038725>
- Jeukenne JP, Lejeune A, Mahaux C (1977) Optical-model potential in finite nuclei from Reid's hard core interaction. *Phys Rev C* 16:80–96, DOI 10.1103/PhysRevC.16.80
- Jose J (2016) *Stellar Explosions: Hydrodynamics and Nucleosynthesis*. CRC Press/Taylor and Francis, DOI 10.1201/b19165
- Junghans AR, de Jong M, Clerc HG, Ignatyuk AV, Kudyaev GA, Schmidt KH (1998) Projectile-fragment yields as a probe for the collective enhancement in the nuclear level density. *Nucl Phys A* 629:635–655, DOI 10.1016/S0375-9474(98)00658-7
- Junghans AR, Rusev G, Schwengner R, Wagner A, Grosse E (2008) Photon data shed new light upon the GDR spreading width in heavy nuclei. *Physics Letters B* 670(3):200–204, DOI 10.1016/j.physletb.2008.10.055, **0810.2268**
- Käppeler F, Gallino R, Bisterzo S, Aoki W (2011) The s process: Nuclear physics, stellar models, and observations. *Rev Mod Phys* 83:157–194, DOI 10.1103/RevModPhys.83.157
- Kirsebom OS, et al (2019) Discovery of an Exceptionally Strong β -Decay Transition of ^{20}F and Implications for the Fate of Intermediate-Mass Stars. *Phys Rev Lett* 123:262701, DOI 10.1103/PhysRevLett.123.262701
- Kullmann I, Goriely S, Just O, Bauswein A, Janka HT (2023) Impact of systematic nuclear uncertainties on composition and decay heat of dynamical and disk ejecta in compact binary mergers. *Mon Not Roy Astron Soc* DOI 10.1093/mnras/stad1458, **2207.07421**
- Lach F, Röpke FK, Seitenzahl IR, Coté B, Gronow S, Ruiter AJ (2020) Nucleosynthesis imprints from different Type Ia supernova explosion scenarios and implications for galactic chemical evolution. *Astron & Astrophys* 644:A118, DOI 10.1051/0004-6361/202038721, **2010.14084**
- Langanke K, Martinez-Pinedo G, Zegers RGT (2021) Electron capture in stars. *Rep Prog Phys* 84(6):066301, DOI 10.1088/1361-6633/abf207, **2009.01750**
- Lejeune A (1980) Low-energy optical model potential in finite nuclei from Reid's hard core interaction. *Phys Rev C* 21(3):1107–1108, DOI 10.1103/PhysRevC.21.1107
- Leung SC, Nomoto K (2021) Type Ia Supernovae and their Explosive Nucleosynthesis: Constraints on Progenitors. arXiv e-prints arXiv:2111.14795, **2111.14795**
- Leung SC, Nomoto K, Suzuki T (2020) Electron-capture Supernovae of Super-AGB Stars: Sensitivity on Input Physics. *Astrophys J* 889(1):34, DOI 10.3847/1538-4357/ab5d2f, **1901.11438**
- Liang H, Litvinova E (2022) Theory of nuclear collective vibrations. arXiv e-prints arXiv:2203.02848, DOI 10.48550/arXiv.2203.02848, **2203.02848**
- Litvinova E, Loens H, Langanke K, Martinez-Pinedo G, Rauscher T, Ring P, Thielemann F, Tselyaev V (2009) Low-lying dipole response in the relativistic quasiparticle time blocking approximation and its influence on neutron capture cross sections. *Nucl Phys A* 823:26–37, DOI 10.1016/j.nuclphysa.2009.03.009
- Liu W, Li Z, He J, Tang X, Lian G, Su J, Shen Y, An Z, Chao F, Chang J, Chen L, Chen H, Chen X, Chen Y, Chen Z, Cheng J, Cui B, Fang X, Fu C, Gan L, Guo B, Han Z, Guo X, He G, He J, Heger A, Hou S, Huang H, Huang N, Jia B, Jiang L, Kubono S, Li J, Li M, Li K, Li E, Li T, Li Y, Lugaro M, Luo X, Ma H, Ma S, Mei D, Nan W, Nan W, Qi N, Qian Y, Qin J, Ren J, Shang C, Sun L, Sun W, Tan W, Tanihata I, Wang S, Wang P, Wang Y, Wu Q, Xu S, Yang Y, Yu X, Yue Q, Zeng S, Zhang L, Zhang H, Zhang H, Zhang L, Zhang N, Zhang P, Zhang Q, Zhang T, Zhang X, Zhang X, Zhao W, Zhou J, Zhou Y (2022) Commissioning of Underground Nuclear Astrophysics Experiment JUNA in China. In: *European Physical Journal Web of Conferences*, vol 260, p 08001, DOI 10.1051/epjconf/202226008001

- Loens H, Langanke K, Martinez-Pinedo G, Rauscher T, Thielemann FK (2008) Complete inclusion of parity-dependent level densities in the statistical description of astrophysical reaction rates. *Phys Lett B* 666:395–399, DOI 10.1016/j.physletb.2008.07.073
- Lynn JE, Back BB (1974) Sub-barrier fission probability for a double-humped barrier. *Journal of Physics A Mathematical General* 7(3):395–409, DOI 10.1088/0305-4470/7/3/011
- Mahaux C, Weidenmuller HA (1979) Recent Developments in Compound-Nucleus Theory. *Annual Review of Nuclear and Particle Science* 29:1–31, DOI 10.1146/annurev.ns.29.120179.000245
- Mamdouh A, Pearson J, Rayet M, Tondeur F (2001) Fission barriers of neutron-rich and superheavy nuclei calculated with the etfsi method. *Nucl Phys A* 679:337–358
- Markova M, von Neumann-Cosel P, Larsen AC, Bassauer S, Gørgen A, Guttormsen M, Bello Garrote FL, Berg HC, Bjørøen MM, Dahl-Jacobsen T, Eriksen TK, Gjestvang D, Isaak J, Mbabane M, Paulsen W, Pedersen LG, Pettersen NIJ, Richter A, Sahin E, Scholz P, Siem S, Tveten GM, Valsdottir VM, Wiedeking M, Zeiser F (2021) Comprehensive Test of the Brink-Axel Hypothesis in the Energy Region of the Pygmy Dipole Resonance. *Phys Rev Lett* 127(18):182501, DOI 10.1103/PhysRevLett.127.182501, [2012.11956](#)
- Martinez-Pinedo G, Mocelj D, Zinner N, Kelic A, Langanke K, Panov I, Pfeiffer B, Rauscher T, Schmidt KH, Thielemann FK (2007) The role of fission in the r-process. *Prog Part Nucl Phys* 59:199–205, DOI 10.1016/j.pnpnp.2007.01.018
- Mathews GJ, Mengoni A, Thielemann FK, Fowler WA (1983) Neutron capture rates in the r-process - The role of direct radiative capture. *Astrophys J* 270:740–745, DOI 10.1086/161164
- McCullagh CM, Stelts ML, Chrien RE (1981) Dipole radiative strength functions from resonance neutron capture. *Phys Rev C* 23(4):1394–1403, DOI 10.1103/PhysRevC.23.1394
- McFadden L, Satchler GR (1966) Optical-model analysis of the scattering of 24.7 MeV alpha particles. *Nucl Phys A* 84:177–200, DOI 10.1016/0029-5582(66)90441-X
- Meisel Z, George S, Ahn S, Bazin D, Brown BA, Browne J, Carpino JF, Chung H, Cyburt RH, Estradé A, Famiano M, Gade A, Langer C, Matoš M, Mittag W, Montes F, Morrissey DJ, Pereira J, Schatz H, Schatz J, Scott M, Shapira D, Smith K, Stevens J, Tan W, Tarasov O, Towers S, Wimmer K, Winkelbauer JR, Yurkon J, Zegers RGT (2020) Nuclear mass measurements map the structure of atomic nuclei and accreting neutron stars. *Phys Rev C* 101(5):052801, DOI 10.1103/PhysRevC.101.052801, [2004.14101](#)
- Mocelj D, Rauscher T, Martinez-Pinedo G, Langanke K, Pacearescu L, Faessler A, Thielemann FK, Alhassid Y (2007) Large-scale prediction of the parity distribution in the nuclear level density and application to astrophysical reaction rates. *Phys Rev C* 75(4):045805, DOI 10.1103/PhysRevC.75.045805, [nucl-th/0703033](#)
- Mohr P, Fülöp Z, Gyürky G, Kiss GG, Szücs T (2020) Successful Prediction of Total α -Induced Reaction Cross Sections at Astrophysically Relevant Sub-Coulomb Energies Using a Novel Approach. *Phys Rev Lett* 124(25):252701, DOI 10.1103/PhysRevLett.124.252701, [2006.03885](#)
- Moldauer PA (1980) Statistics and the average cross section. *Nucl Phys A* 344(2):185–195, DOI 10.1016/0375-9474(80)90671-5
- Möller P, Nix JR, Myers WD, Swiatecki WJ (1995) Nuclear Ground-State Masses and Deformations. *At Data Nucl Data Tables* 59:185, DOI 10.1006/adnd.1995.1002, URL <https://t2.lanl.gov/nis/data/astro/molnix96/massd-FRDM1992.html>
- Möller P, Sierk AJ, Ichikawa T, Iwamoto A, Mumpower M (2015) Fission barriers at the end of the chart of the nuclides. *Phys Rev C* 91(2):024310, DOI 10.1103/PhysRevC.91.024310
- Monpriat E, Martinet S, Courtin S, Heine M, Ekström S, Jenkins DG, Choplin A, Adley P, Curien D, Moukaddam M, Nippert J, Tsiatsiou S, Meynet G (2022) A new $^{12}\text{C} + ^{12}\text{C}$ nuclear reaction rate: Impact on stellar evolution. *Astron & Astrophys* 660:A47, DOI 10.1051/0004-6361/202141858, [2111.15224](#)
- Myers WD, Świątecki WJ (1999) Thomas-fermi fission barriers. *Phys Rev C* 60:014606, DOI 10.1103/PhysRevC.60.014606
- Nakagawa T, Chiba S, Hayakawa T, Kajino T (2005) Maxwellian-averaged neutron-induced reaction cross sections and astrophysical reaction rates for $kT = 1$ keV to 1 MeV calculated from microscopic neutron cross section library JENDL-3.3. *Atomic Data and Nuclear Data Tables* 91(2):77–186, DOI 10.1016/j.adt.2005.08.002

- Nomoto K, Thielemann FK, Miyaji S (1985) The triple alpha reaction at low temperatures in accreting white dwarfs and neutron stars. *Astron & Astrophys* 149(2):239–245
- Ojima T, Ishimaru Y, Wanajo S, Prantzos N, François P (2018) Stochastic Chemical Evolution of Galactic Subhalos and the Origin of r-process Elements. *Astrophys J* 865:87, DOI 10.3847/1538-4357/aada11
- Panov IV, Kolbe E, Pfeiffer B, Rauscher T, Kratz KL, Thielemann FK (2005) Calculations of fission rates for r-process nucleosynthesis. *Nucl Phys A* 747:633–654, DOI 10.1016/j.nuclphysa.2004.09.115
- Panov IV, Korneev IY, Rauscher T, Martinez-Pinedo G, Kelic-Heil A, Zinner NT, Thielemann FK (2010) Neutron-induced astrophysical reaction rates for translead nuclei. *Astron & Astrophys* 513:A61, DOI 10.1051/0004-6361/200911967
- Petermann I, Langanke K, Martinez-Pinedo G, Panov IV, Reinhard PG, Thielemann FK (2012) Have superheavy elements been produced in nature? *Eur Phys J A* 48:122, DOI 10.1140/epja/i2012-12122-6
- Rauscher T (2010) code smaragd. unpublished
- Rauscher T (2011) The Path to Improved Reaction Rates for Astrophysics. *Int J Mod Phys E* 20:1071–1169, DOI 10.1142/S021830131101840X
- Rauscher T (2020) Essentials of Nucleosynthesis and Theoretical Nuclear Astrophysics. 2514-3433, IOP Publishing, DOI 10.1088/2514-3433/ab8737, URL <http://dx.doi.org/10.1088/2514-3433/ab8737>
- Rauscher T (2022) Stellar neutron captures at low and high temperatures. *Eur Phys J A* 58:214, DOI 10.1140/epja/s10050-022-00866-9
- Rauscher T, Thielemann FK (2000) Astrophysical Reaction Rates From Statistical Model Calculations. *At Data Nucl Data Tables* 75:1–351, DOI 10.1006/adnd.2000.0834
- Rauscher T, Thielemann FK, Kratz KL (1997) Nuclear level density and the determination of thermonuclear rates for astrophysics. *Phys Rev C* 56:1613–1625, DOI 10.1103/PhysRevC.56.1613
- Rauscher T, Bieber R, Oberhummer H, Kratz KL, Dobaczewski J, Möller P, Sharma MM (1998) Dependence of direct neutron capture on nuclear-structure models. *Phys Rev C* 57(4):2031–2039, DOI 10.1103/PhysRevC.57.2031, [nuc1-th/9801005](https://arxiv.org/abs/nuc1-th/9801005)
- Rauscher T, Thielemann FK, Görres J, Wiescher M (2000) Capture of α particles by isospin-symmetric nuclei. *Nucl Phys A* 675(3-4):695–721, DOI 10.1016/S0375-9474(00)00182-2, [nuc1-th/0003057](https://arxiv.org/abs/nuc1-th/0003057)
- Rauscher T, Dauphas N, Dillmann I, Fröhlich C, Fülöp Z, Gyürky G (2013) Constraining the astrophysical origin of the p-nuclei through nuclear physics and meteoritic data. *Rep Prog Phys* 76:066201, DOI 10.1088/0034-4885/76/6/066201
- Reichert M, Winteler C, Korobkin O, Arcones A, Bliss J, Eichler M, Frischknecht U, Fröhlich C, Hirschi R, Jacobi M, Kuske J, Martinez-Pinedo G, Martin D, Mocelj D, Rauscher T, Thielemann FK (2023) The nuclear reaction network WinNet. *arXiv e-prints arXiv:2305.07048*, DOI 10.48550/arXiv.2305.07048, [2305.07048](https://arxiv.org/abs/2305.07048)
- Roberti L, Pignatari M, Psaltis A, Sieverding A, Mohr P, Fülöp Z, Lugaro M (2023) The γ -process nucleosynthesis in core-collapse supernovae. I. A novel analysis of γ -process yields in massive stars. *arXiv e-prints arXiv:2306.11409*, DOI 10.48550/arXiv.2306.11409, [2306.11409](https://arxiv.org/abs/2306.11409)
- Rolfs C, Rodney W (1988) *Cauldrons in the Cosmos: Nuclear Astrophysics*. University of Chicago Press, Chicago
- Satchler GR, Love WG (1979) Folding model potentials from realistic interactions for heavy-ion scattering. *Phys Rep* 55(3):183–254, DOI 10.1016/0370-1573(79)90081-4
- Schatz H, Ong WJ (2017) Dependence of X-Ray Burst Models on Nuclear Masses. *Astrophys J* 844(2):139, DOI 10.3847/1538-4357/aa7de9, [1610.07596](https://arxiv.org/abs/1610.07596)
- Schatz H, Aprahamian A, Goerres J, Wiescher M, Rauscher T, Rembges JF, Thielemann FK, Pfeiffer B, Moeller P, Kratz KL, Herndl H, Brown BA, Rebel H (1998) rp-Process Nucleosynthesis at Extreme Temperature and Density Conditions. *Phys Rep* 294:167–264, DOI 10.1016/S0370-1573(97)00048-3

- Schatz H, Becerril Reyes AD, Best A, Brown EF, Chatziioannou K, Chipps KA, Deibel CM, Ezzeddine R, Galloway DK, Hansen CJ, Herwig F, Ji AP, Lugaro M, Meisel Z, Norman D, Read JS, Roberts LF, Spyrou A, Tews I, Timmes FX, Travaglio C, Vassh N, Abia C, Adsley P, Agarwal S, Aliotta M, Aoki W, Arcones A, Aryan A, Bandyopadhyay A, Banu A, Bardayan DW, Barnes J, Bauswein A, Beers TC, Bishop J, Boztepe T, Cote B, Caplan ME, Champagne AE, Clark JA, Couder M, Couture A, de Mink SE, Debnath S, deBoer RJ, den Hartogh J, Denissenkov P, Dexheimer V, Dillmann I, Escher JE, Famiano MA, Farmer R, Fisher R, Fröhlich C, Frebel A, Fryer C, Fuller G, Ganguly AK, Ghosh S, Gibson BK, Gorda T, Gourgouliatos KN, Graber V, Gupta M, Haxton WC, Heger A, Hix WR, Ho WCG, Holmbeck EM, Hood AA, Huth S, Imbriani G, Izzard RG, Jain R, Jayatissa H, Johnston Z, Kajino T, Kankainen A, Kiss GG, Kwiatkowski A, La Cognata M, Laird AM, Lamia L, Landry P, Laplace E, Launey KD, Leahy D, Leckenby G, Lennarz A, Longfellow B, Lovell AE, Lynch WG, Lyons SM, Maeda K, Masha E, Matei C, Merc J, Messer B, Montes F, Mukherjee A, Mumpower MR, Neto D, Nevins B, Newton WG, Nguyen LQ, Nishikawa K, Nishimura N, Nunes FM, O'Connor E, O'Shea BW, Ong WJ, Pain SD, Pajkos MA, Pignatari M, Pizzone RG, Placco VM, Plewa T, Pritychenko B, Psaltis A, Puentes D, Qian YZ, Radice D, Rapagnani D, Rebeiro BM, Reifarth R, Richard AL, Rijal N, Roederer IU, Rojo JS, J S K, Saito Y, Schwenk A, Sergi ML, Sidhu RS, Simon A, Sivarani T, Skuladottir Á, Smith MS, Spiridon A, Sprouse TM, Starrfield S, Steiner AW, Strieder F, Sultana I, Surman R, Szücs T, Tawfik A, Thielemann F, Trache L, Trappitsch R, Tsang MB, Tumino A, Upadhyayula S, Valle Martinez JO, Van der Swaelmen M, Viscasillas Vazquez C, Watts A, Wehmeyer B, Wiescher M, Wrede C, Yoon J, Zegers RGT, Zermare MA, Zingale M (2022) Horizons: nuclear astrophysics in the 2020s and beyond. *J Phys G: Nucl Part Phys* 49(11):110502, DOI 10.1088/1361-6471/ac8890, [2205.07996](#)
- Schunck N, Regnier D (2022) Theory of nuclear fission. *Progress in Particle and Nuclear Physics* 125:103963, DOI 10.1016/j.ppnp.2022.103963, [2201.02719](#)
- Sieja K (2018) Shell-model study of the $M1$ dipole strength at low energy in the $A > 100$ nuclei. *Phys Rev C* 98:064,312, DOI 10.1103/PhysRevC.98.064312
- Soppera N, Bossant M, Dupont E, Henriksson H, Rugawa Y (2011) Recent Upgrades to the Nuclear Data Tool JANIS. *J Korean Phys Soc* 59:1329–1332, DOI 10.3938/jkps.59.1329
- Strutinsky VM (1967) Shell effects in nuclear masses and deformation energies. *Nucl Phys A* 95(2):420–442, DOI 10.1016/0375-9474(67)90510-6
- Strutinsky VM (1968) “Shells” in deformed nuclei. *Nucl Phys A* 122(1):1–33, DOI 10.1016/0375-9474(68)90699-4
- Tang X, Ru L (2022) The $^{12}\text{C}+^{12}\text{C}$ fusion reaction at stellar energies. In: *European Physical Journal Web of Conferences, European Physical Journal Web of Conferences*, vol 260, p 01002, DOI 10.1051/epjconf/202226001002
- Tepel JW, Hofmann HM, Weidenmüller HA (1974) Hauser-Feshbach formulas for medium and strong absorption. *Physics Letters B* 49(1):1–4, DOI 10.1016/0370-2693(74)90565-6
- Thielemann FK, Arnett WD (1985) Hydrostatic Nucleosynthesis - Part Two - Core Neon to Silicon Burning and Presupernova Abundance Yields of Massive Stars. *Astrophys J* 295:604, DOI 10.1086/163403
- Thielemann FK, Arnould M (1983) Average radiation widths and the giant dipole resonance width. In: Böckhoff KH (ed) *Nuclear Data for Science and Technology*, Springer Netherlands, Dordrecht, pp 762–765
- Thielemann FK, Metzinger J, Klapdor HV (1983) Beta-delayed fission and neutron emission: Consequences for the astrophysical r-process and the age of the galaxy. *Zeitschrift für Phys A: Hadrons and Nuclei* 309:301–317, DOI 10.1007/BF01413833
- Thielemann FK, Arnould M, Truran JW (1986) Thermonuclear reaction rates from statistical model calculations. In: Vangioni-Flam E, Audouze J, Casse M, Chieze JP, Tran Thanh Van J (eds) *Advances in Nuclear Astrophysics*, pp 525–540
- Thielemann FK, Heger A, Hirschi R, Liebendörfer M, Diehl R (2018) Massive Stars and Their Supernovae. In: Diehl R, Hartmann DH, Prantzos N (eds) *Astrophysics with Radioactive Isotopes*, Berlin Springer Verlag, vol 453, pp 173–286

- Thomas J, Zirnbauer MR, Langanke K (1986) $^{26}\text{Al}(n,p)^{26}\text{Mg}$ reaction: Comparison between the Hauser-Feshbach formula and the exact random-matrix result for the cross section. *Phys Rev C* 33(6):2197–2199, DOI 10.1103/PhysRevC.33.2197
- Tiesinga E, Mohr PJ, Newell DB, Taylor BN (2021) CODATA recommended values of the fundamental physical constants: 2018*. *Reviews of Modern Physics* 93(2):025010, DOI 10.1103/RevModPhys.93.025010
- Timmes FX (1999) Integration of Nuclear Reaction Networks for Stellar Hydrodynamics. *Astrophys J Suppl* 124:241–263, DOI 10.1086/313257
- Truran JW, Hansen CJ, Cameron AGW, Gilbert A (1966) Thermonuclear reactions in medium and heavy nuclei. *Canadian Journal of Physics* 44:151, DOI 10.1139/p66-011
- Tursunov EM, Turakulov SA, Kadyrov AS, Blokhintsev LD (2021) Astrophysical S factor and rate of $^7\text{Be}(p,\gamma)^8\text{B}$ direct capture reaction in a potential model. *Phys Rev C* 104(4):045806, DOI 10.1103/PhysRevC.104.045806, [2105.11091](#)
- van Isacker P, Nagarajan MA, Warner DD (1992) Effect of the neutron skin on collective states of nuclei. *Phys Rev C* 45(1):R13–R16, DOI 10.1103/PhysRevC.45.R13
- Vasini A, Matteucci F, Spitoni E (2022) Chemical evolution of ^{26}Al and ^{60}Fe in the Milky Way. *Mon Not Roy Astron Soc* 517(3):4256–4264, DOI 10.1093/mnras/stac2981, [2204.00510](#)
- Vasini A, Matteucci F, Spitoni E, Siegert T (2023) Evolution of radioactive elements in the LMC: predictions for future γ -ray surveys. *Mon Not Roy Astron Soc* 523(1):1153–1162, DOI 10.1093/mnras/stad1440, [2305.04753](#)
- Vassh N, Vogt R, Surman R, Randrup J, Sprouse TM, Mumpower MR, Jaffke P, Shaw D, Holmbeck EM, Zhu Y, McLaughlin GC (2019) Using excitation-energy dependent fission yields to identify key fissioning nuclei in r-process nucleosynthesis. *J Phys G: Nucl Part Phys* 46:065,202, DOI 10.1088/1361-6471/ab0bea
- Wanajo S, Janka HT, Kubono S (2011) Uncertainties in the νp -process: Supernova Dynamics Versus Nuclear Physics. *Astrophys J* 729(1):46, DOI 10.1088/0004-637X/729/1/46, [1004.4487](#)
- Ward RA, Fowler WA (1980) Thermalization of long-lived nuclear isomeric states under stellar conditions. *Astrophys J* 238:266–286, DOI 10.1086/157983
- Wiescher M, Gorres J, Thielemann FK, Ritter H (1986) Explosive hydrogen burning in novae. *Astron & Astrophys* 160:56–72
- Woosley SE, Arnett WD, Clayton DD (1973) The Explosive Burning of Oxygen and Silicon. *Astrophys J Suppl* 26:231, DOI 10.1086/190282
- Woosley SE, Fowler WA, Holmes JA, Zimmerman BA (1978) Semiempirical Thermonuclear Reaction-Rate Data for Intermediate-Mass Nuclei. *At Data Nucl Data Tables* 22:371, DOI 10.1016/0092-640X(78)90018-9